Contents lists available at ScienceDirect

International Journal of Solids and Structures

Micromorphic approach to phase-field modeling of multivariant martensitic transformation with rate-independent dissipation effects

Mohsen Rezaee-Hajidehi, Stanisław Stupkiewicz *

Institute of Fundamental Technological Research (IPPT), Polish Academy of Sciences, Pawińskiego 5B, 02-106 Warsaw, Poland

A B S T R A C T

A micromorphic formulation of the phase-field model of martensitic transformation is developed within the incremental energy minimization framework. In contrast to the conventional phase-field formulation, the order parameters are viewed as local variables and the corresponding evolution equations are solved at the material-point level, i.e. at the Gauss points in the finite-element setting. From a computational standpoint, such a treatment is advantageous for complex evolution laws that may lead to computational difficulties if treated globally, as in the conventional phase-field formulation. In the micromorphic formulation, each order parameter is coupled to its micromorphic counterpart governed by a global Helmholtz-type PDE. This coupling ensures that the interfacial energy and related size effects are correctly captured by the model. In this work, the micromorphic approach is applied to a finite-strain multivariant phase-field model that incorporates rate-independent dissipation. The augmented Lagrangian technique is then used to transform the resulting non-smooth incremental minimization problem to a smooth and unconstrained saddle-point problem. Microstructure evolution under nano-indentation is studied to illustrate the approach.

© 2021 The Author(s). Published by Elsevier Ltd. This is an open access article under the CC BY license (http://creativecommons.org/licenses/by/4.0/).

1. Introduction

Phase-field method is a versatile computational approach that allows to simulate complex microstructure patterns. The basic idea of the method is to replace sharp interfaces, which can be computationally troublesome to be tracked, by spatially diffuse interfaces. This is achieved by introducing continuous variables, called order parameters, the gradients of which are explicit arguments of the free energy function, thus providing a continuum description of the interfacial energy. Modeling the microstructure evolution in martensitic phase transformation is one of the early applications of the phase-field method, as rooted in the pioneering works of Wang and Khachaturyan (1997), Artemev et al. (2000), Wen et al. (2000), Levitas and Preston (2002), and has been the subject of a great number of studies based on the spectral solvers (e.g., Ahluwalia et al., 2004; Shu and Yen, 2008; Borukhovich et al., 2014; Zhong and Zhu, 2014; Zhao et al., 2020) and on the finite-element method (e.g., Bartels and Mosler, 2017; Clayton and Knap, 2011; Hildebrand and Miehe, 2012; Levitas et al., 2009;

Schmitt et al., 2013; She et al., 2013; Tůma et al., 2016, 2021). The latter framework is employed in this work.

The standard phase-field formulation for modeling the microstructure evolution leads to a coupled problem of mechanical equilibrium (with displacements as the primary unknowns) and viscous evolution of the order parameters. In the conventional format, the problem is solved on the global level, simultaneously with respect to all unknowns. In the case of more complex evolution laws, the conventional solution procedure can be restrictive and may not lead to computationally efficient formulations. A possible remedy would be to shift the complexities from the global level to the local one. This can be done straightforwardly by using the micromorphic approach.

The main idea of the micromorphic approach, in line with Forest (2009), lies in the introduction of additional degrees of freedom (of any type and tensorial order, depending on the context), which are the micromorphic counterparts of selected internal variables. The coupling between the micromorphic variables and the original ones is then provided via the penalty method. Following this modification, the gradients of the original variables in the constitutive equations are replaced by the gradients of their micromorphic counterparts. Accordingly, the original variables can be viewed as local quantities and the corresponding governing equations can be solved at the local level, e.g. at each Gauss point in the

---

* Corresponding author.

E-mail addresses: mrezaee@ippt.pan.pl (M. Rezaee-Hajidehi), sstupkie@ippt.pan.pl (S. Stupkiewicz).

finite-element setting. For a general description of the micromorphic approach the reader is referred to Forest (2009), see also Forest (2016).

Due to its generality, the micromorphic approach can be employed to virtually any gradient model, such as gradient plasticity (Anand et al., 2012; Mazière and Forest, 2015) and crystal plasticity (Aslan et al., 2011; Wulfinghoff and Böhlke, 2012; Ryś et al., 2020), gradient-enhanced continuum damage (Dimitrijevic and Hackl, 2008; Waffenschmidt et al., 2014; Poh and Sun, 2017), and gradient-enhanced pseudoelasticity (Rezaee-Hajidehi and Stupkiewicz, 2018; Rezaee-Hajidehi et al., 2020). Applications of the micromorphic approach in the context of phase-field modeling are scarce. It has been used by Miehe et al. (2016, 2017) to facilitate the finite-element implementation of their phase-field model of ductile fracture (coupled damage and plasticity). The micromorphic approach has been also employed by Di Leo et al. (2014) in their Cahn–Hilliard-type phase-field model of species diffusion coupled with large elastic deformations, with the aim to reduce a fourth-order PDE to two second-order PDEs to be amenable to finite-element discretization, see also Ubachs et al. (2004).

In this work, the micromorphic approach is applied to a finite-strain phase-field model of multivariant martensitic phase transformation in shape memory alloys. In the case of a viscous-type evolution, for which the corresponding conventional phase-field formulation has been developed by Rezaee-Hajidehi and Stupkiewicz (2020), the micromorphic regularization is straightforward, however, it does not bring any computational advantages with respect to the conventional formulation. On the other hand, when rate-independent dissipation effects are accounted for, the conventional formulation does not lead to a computationally efficient finite-element implementation. Accordingly, the role of the micromorphic regularization becomes particularly important, as it allows to shift the complexities induced by the rate-independent dissipation to the local level where they can be treated in an efficient and robust manner. Specifically, the augmented Lagrangian method is used in this work to handle the non-smoothness introduced by the rate-independent dissipation, and it is shown that, in this context, the micromorphic formulation performs much better than the conventional one.

The variational formulation employed in this work is derived from the general incremental energy minimization framework. In this approach, the solution of the evolution problem is found by minimizing the incremental energy supplied to the system which is equal to the sum of incremental free energy and dissipation complemented by the increment of the external loading potential. Starting from the conditions of stability in rate-independent plasticity, the incremental energy minimization framework has been developed by Henryk Petryk in a series of seminal papers (Petryk, 1982, 1985, 1991, 1993, 2003), later extended, for instance, to account for the interfacial energy effects (Petryk and Stupkiewicz, 2010), including stability of evolving laminates (Petryk and Stupkiewicz, 2012), and recently extended to non-potential problems (Petryk, 2020). Other developments and applications of this general framework can be found in numerous works (e.g., Ortiz and Repetto, 1999; Carstensen et al., 2002; Miehe et al., 2004; Kružík et al., 2005; Miehe, 2011; Mielke and Roubíček, 2015). The incremental energy minimization framework has been also employed in the context of the phase-field method. The corresponding variational formulation adopted in this work is based on that developed by Hildebrand and Miehe (2012), and later extended to constrained evolution by Tůma et al. (2016) and to mixed-type dissipation with rate-independent dissipation effects by Tůma et al. (2018).

One of the beneficial features of the phase-field method is that most of the material parameters involved in the model have a clear physical interpretation and can be, at least in principle, determined

independently. On the other hand, parameters with a more phenomenological nature (e.g., the mobility parameters) can be identified through small-scale testing, for instance, using nano-indentation, which is considered as a model problem in this work. The simulations are here limited to 2D problems which, despite the related simplifications, may deliver valuable qualitative predictions. As an example, the indentation size effect due to interfacial energy effects has been studied in our recent work (Rezaee-Hajidehi and Stupkiewicz, 2020). More realistic 3D phase-field simulations of nano-indentation necessarily involve large-scale simulations and are so far limited to the conventional formulation with viscous dissipation (Tůma et al., 2021).

This paper is organized as follows. In Section 2, a simple prototype small-strain phase-field model and its micromorphic regularization are presented in order to elucidate the structure of the micromorphic formulation. A finite-strain multivariant extension of the model is then presented in Section 3.1 and its micromorphic regularization in Section 3.2. The model is based on the elastic strain energy of Hencky type, double-obstacle potential, and penalty regularization of the inequality constraints on the order parameters. In Section 3.3, the model is extended to incorporate a mixed-type dissipation, i.e. a combination of the viscous and rate-independent dissipation contributions, as a result of which the incremental minimization problem becomes non-smooth. To treat the non-smoothness, an augmented Lagrangian formulation is developed which leads to an equivalent smooth and unconstrained saddle-point problem, see Appendix A. The details of the finite-element implementation are presented in Section 4. Finally, illustrative 2D examples are presented in Section 5, where the microstructure evolution during nano-indentation has been chosen as a model problem. In particular, the computational benefits delivered by the micromorphic regularization are highlighted for a simple system with one order parameter, see Section 5.2, while the physical aspects of the rate-independent dissipation are illustrated in Sections 5.3 and 5.4 for a multivariant transformation.

2. A prototype phase-field model

To illustrate the idea of the micromorphic regularization, let us consider a possibly simple prototype model for a system involving only two phases. The model is formulated in the small-strain setting and includes a single non-conserved order parameter η, interpreted as the relative phase volume fraction, the evolution of which is governed by the classical Ginzburg–Landau equation (e.g., Penrose and Fife, 1990),

$$\dot{\eta} = -m \frac{\delta \mathcal{F}}{\delta \eta}, \qquad \frac{\delta \mathcal{F}}{\delta \eta} = \frac{\partial F}{\partial \eta} - \nabla \cdot \frac{\partial F}{\partial \nabla \eta}. \tag{1}$$

The superimposed dot denotes here the (material) time derivative, m is the mobility parameter and $\delta \mathcal{F}/\delta \eta$ is the variational derivative of the functional $\mathcal{F}$ of the total Helmholtz free energy of the density F (to be specified later).

Following the variational approach of Hildebrand and Miehe (2012), see also Miehe (2011); Tůma et al. (2016), we first formulate the governing equations of the conventional phase-field model in the rate form, Section 2.1, and then develop its incremental (time-discrete) version, Section 2.2. In Section 2.3, we introduce the micromorphic approach (Forest, 2009; Forest, 2016) and develop the micromorphic regularization of the conventional model. This set of prototype models lays the ground for the subsequent development of the model to more complex scenarios.

2.1. Variational formulation of the rate-problem

In the case of transformation involving two phases, the phase composition can be described by a single order parameter η such that $\eta = 0$ and $\eta = 1$ correspond to the pure phases, and the intermediate values correspond to diffuse interfaces. The complete system is thus described by two continuous fields, the displacement vector $\mathbf{u}$ and the scalar order parameter η, defined over the entire body domain B. The strain tensor $\boldsymbol{\varepsilon} = \nabla_s \mathbf{u} = \frac{1}{2}\left(\nabla \mathbf{u} + (\nabla \mathbf{u})^{\mathrm{T}}\right)$ is additively split into the elastic part $\boldsymbol{\varepsilon}^{\mathrm{e}}$ and the transformation part $\boldsymbol{\varepsilon}^{\mathrm{t}}$, i.e. $\boldsymbol{\varepsilon} = \boldsymbol{\varepsilon}^{\mathrm{e}} + \boldsymbol{\varepsilon}^{\mathrm{t}}$.

The Helmholtz free energy functional $\mathcal{F}$ is defined as the integral of the density F over domain B,

$$\mathcal{F}[\mathbf{u}, \eta] = \int_B F(\nabla_s \mathbf{u}, \eta, \nabla \eta) \, dV, \tag{2}$$

where F comprises the chemical energy F_{chem}, the elastic strain energy F_{el} and the interfacial energy F_{int},

$$F(\boldsymbol{\varepsilon}, \eta, \nabla \eta) = F_{\mathrm{chem}}(\eta) + F_{\mathrm{el}}(\boldsymbol{\varepsilon}, \eta) + F_{\mathrm{int}}(\eta, \nabla \eta). \tag{3}$$

In the adopted notation, square brackets and parentheses are used to distinguish the arguments of, respectively, functionals and functions.

The chemical energy F_{chem} is defined as

$$F_{\mathrm{chem}}(\eta) = (1 - \eta)F_1^0 + \eta F_2^0, \tag{4}$$

where the constants F_1^0 and F_2^0 represent the chemical energy of the individual phases. The elastic strain energy is expressed as,

$$F_{\mathrm{el}}(\boldsymbol{\varepsilon}, \eta) = \frac{1}{2}\left(\boldsymbol{\varepsilon} - \boldsymbol{\varepsilon}^{\mathrm{t}}(\eta)\right) \cdot \mathbb{L}\left(\boldsymbol{\varepsilon} - \boldsymbol{\varepsilon}^{\mathrm{t}}(\eta)\right), \tag{5}$$

where the transformation strain $\boldsymbol{\varepsilon}^{\mathrm{t}}$ is obtained by averaging the transformation strains of pure phases $\boldsymbol{\varepsilon}_1^{\mathrm{t}}$ and $\boldsymbol{\varepsilon}_2^{\mathrm{t}}$, i.e. $\boldsymbol{\varepsilon}^{\mathrm{t}}(\eta) = (1 - \eta)\boldsymbol{\varepsilon}_1^{\mathrm{t}} + \eta \boldsymbol{\varepsilon}_2^{\mathrm{t}}$, and $\mathbb{L}$ represents the elastic stiffness tensor, which is assumed constant. The interfacial energy F_{int} takes the form of a double-well potential (Steinbach, 2009),

$$F_{\mathrm{int}}(\eta, \nabla \eta) = \frac{6\gamma}{\ell}\left(\eta^2(1 - \eta)^2 + \frac{\ell^2}{4}\nabla \eta \cdot \nabla \eta\right), \tag{6}$$

where γ represents the interfacial energy density (per unit area) and ℓ characterizes the thickness of the diffuse interface.

A global variational formulation will be now developed following Hildebrand and Miehe (2012) and Tůma et al. (2016). To this end, the potential energy functional $\mathcal{E}$ is defined as

$$\mathcal{E}[\mathbf{u}, \eta] = \mathcal{F}[\mathbf{u}, \eta] + \Omega[\mathbf{u}], \tag{7}$$

where Ω is the potential of external loads (assumed conservative). The global rate-potential is then formulated by adding the global dissipation potential $\mathcal{D}$ to the rate-functional $\dot{\mathcal{E}} = d\mathcal{E}/dt$,

$$\Pi[\dot{\mathbf{u}}, \dot{\eta}; \mathbf{u}, \eta] = \dot{\mathcal{E}}[\dot{\mathbf{u}}, \dot{\eta}; \mathbf{u}, \eta] + \mathcal{D}[\dot{\eta}], \tag{8}$$

where the dissipation is here assumed to be of a purely viscous nature, i.e. the local dissipation potential D is quadratic in the rate of η,

$$\mathcal{D}[\dot{\eta}] = \int_B D(\dot{\eta}) \, dV, \qquad D(\dot{\eta}) = D^{\mathrm{v}}(\dot{\eta}) = \frac{1}{2m}\dot{\eta}^2. \tag{9}$$

Finally, the complete evolution problem is expressed as the minimization of the global rate-potential Π with respect to $\dot{\mathbf{u}}$ and $\dot{\eta}$,

$$\{\dot{\mathbf{u}}, \dot{\eta}\} = \arg\min_{\dot{\mathbf{u}}, \dot{\eta}} \ \Pi[\dot{\mathbf{u}}, \dot{\eta}; \mathbf{u}, \eta]. \tag{10}$$

Minimization of Π with respect to $\dot{\mathbf{u}}$ reduces to the stationarity of $\dot{\mathcal{E}}$ with respect to any kinematically admissible variation $\delta\dot{\mathbf{u}}$, viz.

$$0 = \delta_{\dot{\mathbf{u}}}\dot{\mathcal{E}}[\dot{\mathbf{u}}, \dot{\eta}; \mathbf{u}, \eta] \qquad \forall \delta\dot{\mathbf{u}}, \tag{11}$$

which yields the weak form of mechanical equilibrium, i.e. the virtual work principle. Note that the virtual work principle (11) is actually formulated in terms of the displacement $\mathbf{u}$ rather than velocity $\dot{\mathbf{u}}$, since $\dot{\mathcal{E}}$ is linear in $\dot{\mathbf{u}}$ (Tůma et al., 2016). Stationarity of Π with respect to any admissible variation of $\dot{\eta}$ leads to the evolution equation for η in weak form, which upon application of the Gauss theorem gives the Ginzburg–Landau equation in the local form (1) (Hildebrand and Miehe, 2012; Tůma et al., 2016).

2.2. Time-discrete formulation

The rate evolution problem described above is now reformulated in a finite-step incremental setting. It is assumed that the solution $(\mathbf{u}_n, \eta_n)$ at the previous time step t_n is known, and the fields $(\mathbf{u}_{n+1}, \eta_{n+1})$ at the current time step $t_{n+1} = t_n + \tau$ are to be found. Hereinafter, for a concise notation, the subscript $n+1$ denoting the quantities at the current time step is removed.

Upon applying the backward Euler method, the global rate-potential Π, Eq. (8), at time t_{n+1} is approximated as

$$\Pi[\dot{\mathbf{u}}, \dot{\eta}; \mathbf{u}, \eta] \approx \frac{1}{\tau}(\mathcal{E}[\mathbf{u}, \eta] - \mathcal{E}[\mathbf{u}_n, \eta_n]) + \mathcal{D}[(\eta - \eta_n)/\tau]. \tag{12}$$

Accordingly, referring to the rate problem (10), the minimization is now performed with respect to $(\mathbf{u}, \eta)$, which is written in the form of the following incremental energy minimization problem,

$$\{\mathbf{u}, \eta\} = \arg\min_{\mathbf{u}, \eta} \ \Pi_\tau[\mathbf{u}, \eta] \tag{13}$$

with the incremental potential Π_τ defined as

$$\Pi_\tau[\mathbf{u}, \eta] = \mathcal{E}[\mathbf{u}, \eta] - \mathcal{E}[\mathbf{u}_n, \eta_n] + \mathcal{D}_\tau[\eta], \tag{14}$$

and with the time-discrete dissipation potential $\mathcal{D}_\tau$ defined in the following form,

$$\mathcal{D}_\tau[\eta] = \int_B D_\tau(\eta) \, dV,$$
$$D_\tau(\eta) = \tau D\left(\frac{\eta - \eta_n}{\tau}\right) = \frac{\tau}{2m}\left(\frac{\eta - \eta_n}{\tau}\right)^2. \tag{15}$$

Stationarity of Π_τ with respect to $\mathbf{u}$ leads to the weak form of mechanical equilibrium (virtual work principle). It is provisionally assumed here that the potential of the external load is defined in the form $\Omega[\mathbf{u}] = -\int_{\partial B_t} \mathbf{t} \cdot \mathbf{u} \, dS$, with $\mathbf{t}$ as the traction prescribed over the boundary ∂B_t. Thus we have

$$0 = \delta_{\mathbf{u}}\Pi_\tau[\mathbf{u}, \eta] = \int_B \boldsymbol{\sigma} \cdot \nabla_s \delta\mathbf{u} \, dV - \int_{\partial B_t} \mathbf{t} \cdot \delta\mathbf{u} \, dS \qquad \forall \delta\mathbf{u}, \tag{16}$$

where $\boldsymbol{\sigma} = \partial F/\partial \boldsymbol{\varepsilon}$ is the stress tensor. Following the standard procedure, the strong from of the mechanical equilibrium is recovered as

$$\nabla \cdot \boldsymbol{\sigma} = \mathbf{0} \quad \text{in } B, \qquad \boldsymbol{\sigma}\mathbf{n} = \mathbf{t} \quad \text{on } \partial B_t, \tag{17}$$

where $\mathbf{n}$ denotes the unit outward normal.

On the other hand, stationarity of Π_τ with respect to η leads to the time-discrete evolution equation for η in the following weak form,

$$0 = \delta_\eta \Pi_\tau[\mathbf{u}, \eta] = \int_B \left(\left(\frac{\partial F}{\partial \eta} + \frac{\partial D_\tau}{\partial \eta}\right)\delta\eta + \frac{\partial F}{\partial \nabla \eta} \cdot \nabla \delta\eta\right) dV \qquad \forall \delta\eta. \tag{18}$$

By applying the Gauss theorem and taking into account the homogeneous Neumann boundary condition $\nabla \eta \cdot \mathbf{n} = 0$ on the whole boundary ∂B, the weak form (18) retrieves the local Ginzburg–Lan-

dau equation (1) under the approximation $\dot{\eta} \approx (\eta - \eta_n)/\tau$ and with $\delta\mathcal{F}/\delta\eta$ given by

$$\frac{\delta\mathcal{F}}{\delta\eta} = \Delta F^0 - \boldsymbol{\sigma} \cdot \Delta\boldsymbol{\varepsilon}^{\mathrm{t}} + \frac{12\gamma}{\ell}\eta(1-\eta)(1-2\eta) - 3\gamma\ell\nabla^2\eta, \qquad (19)$$

where $\Delta F^0 = F_2^0 - F_1^0$ and $\Delta\boldsymbol{\varepsilon}^{\mathrm{t}} = \boldsymbol{\varepsilon}_2^{\mathrm{t}} - \boldsymbol{\varepsilon}_1^{\mathrm{t}}$. The time-discrete Ginzburg–Landau equation is thus a PDE with the order parameter η as the unknown, which is coupled with the displacement $\mathbf{u}$ through the stress $\boldsymbol{\sigma}$ in the driving force, Eq. (19).

2.3. Micromorphic regularization

The classical phase-field model presented above is now cast in the context of the micromorphic framework (Forest, 2009, 2016). To this end, a new variable χ, the micromorphic counterpart of the order parameter η is introduced and the gradient $\nabla\eta$ is replaced by $\nabla\chi$. The coupling between η and χ is then provided by an additional penalization term in the Helmholtz free energy. Coupling the two fields using Lagrange multipliers could be considered as an alternative approach (e.g., Scherer et al., 2020), which, however, is not pursued here since the penalty-based micromorphic approach performs satisfactorily, as shown in Section 5.

With reference to Eq. (2), the Helmholtz free energy F is modified as,

$$F(\boldsymbol{\varepsilon}, \eta, \chi, \nabla\chi) = F_{\mathrm{chem}}(\eta) + F_{\mathrm{el}}(\boldsymbol{\varepsilon}, \eta) + F_{\mathrm{int}}(\eta, \nabla\chi) + F_\mu(\eta, \chi). \qquad (20)$$

The term F_μ penalizes the difference between η and χ,

$$F_\mu(\eta, \chi) = \frac{1}{2}\epsilon_\mu(\eta - \chi)^2, \qquad (21)$$

with the penalty parameter $\epsilon_\mu > 0$. It is stressed that the interfacial energy F_{int}, given by Eq. (6), is now expressed in terms of $\nabla\chi$ instead of $\nabla\eta$.

Next, the evolution problem (10) is reformulated in the micromorphic framework. We will skip the presentation of the rate-problem and only formulate the problem in the incremental form. In analogy to Eq. (13), we have

$$\{\mathbf{u}, \eta, \chi\} = \arg\min_{\mathbf{u}, \eta, \chi} \ \Pi_\tau[\mathbf{u}, \eta, \chi], \qquad (22)$$

with the incremental potential Π_τ defined accordingly, see Eqs. (14), (7) and (2).

However, as a result of the micromorphic regularization, the Helmholtz free energy F, Eq. (20), depends only on η and not on its gradient. Accordingly, η can be viewed as a local quantity, and thus can be determined locally at each material point. The evolution of η is thus governed by the following local (pointwise) minimization problem,

$$\eta = \arg\min_\eta \ \pi_\tau(\boldsymbol{\varepsilon}, \eta, \chi, \nabla\chi), \qquad (23)$$

where $\boldsymbol{\varepsilon}, \chi$ and $\nabla\chi$ are fixed, and the local incremental potential π_τ is expressed as

$$\pi_\tau(\boldsymbol{\varepsilon}, \eta, \chi, \nabla\chi) = F(\boldsymbol{\varepsilon}, \eta, \chi, \nabla\chi) - F(\boldsymbol{\varepsilon}_n, \eta_n, \chi_n, \nabla\chi_n) + D_\tau(\eta). \qquad (24)$$

The condition of stationarity of π_τ with respect to η yields the evolution equation for η in the form of the Ginzburg–Landau equation (1) with $\dot{\eta} \approx (\eta - \eta_n)/\tau$ and

$$\frac{\delta\mathcal{F}}{\delta\eta} = \frac{\partial F}{\partial\eta} = \Delta F^0 - \boldsymbol{\sigma} \cdot \Delta\boldsymbol{\varepsilon}^{\mathrm{t}} + \frac{12\gamma}{\ell}\eta(1-\eta)(1-2\eta) + \epsilon_\mu(\eta - \chi). \qquad (25)$$

It follows that, as a result of the micromorphic regularization, the driving force for transformation involves now the term

$\epsilon_\mu(\eta - \chi)$ which replaces the term with the Laplacian of η in Eq. (19). Accordingly, the minimization problem (23) can be solved locally, which yields η as a function of $\boldsymbol{\varepsilon}$ and χ (note that η does not explicitly depend on $\nabla\chi$, cf. Eq. (25)). A reduced incremental potential π_τ^{red} can thus be defined,

$$\pi_\tau^{\mathrm{red}}(\boldsymbol{\varepsilon}, \chi, \nabla\chi) = \min_\eta \ \pi_\tau(\boldsymbol{\varepsilon}, \eta, \chi, \nabla\chi). \qquad (26)$$

The global variables $\mathbf{u}$ and χ are then governed by minimization of the reduced global potential Π_τ^{red},

$$\{\mathbf{u}, \chi\} = \arg\min_{\mathbf{u}, \chi} \ \Pi_\tau^{\mathrm{red}}[\mathbf{u}, \chi], \qquad (27)$$

where

$$\Pi_\tau^{\mathrm{red}}[\mathbf{u}, \chi] = \int_B \pi_\tau^{\mathrm{red}}(\nabla_s\mathbf{u}, \chi, \nabla\chi)\,\mathrm{d}V + \Delta\Omega[\mathbf{u}]. \qquad (28)$$

As in the case of the conventional phase-field model, minimization of Π_τ^{red} with respect to the displacement field $\mathbf{u}$ leads to the mechanical equilibrium, see Eqs. (16) and (17). Minimization of Π_τ^{red} with respect to χ yields the stationarity condition,

$$0 = \delta_\chi\Pi_\tau^{\mathrm{red}}[\mathbf{u}, \chi] = \int_B \big(3\gamma\ell\nabla\chi \cdot \nabla\delta\chi - \epsilon_\mu(\eta - \chi)\delta\chi\big)\,\mathrm{d}V \qquad \forall\delta\chi, \qquad (29)$$

which is a weak form of the following Helmholtz-type PDE,

$$\chi - \ell_\mu^2\nabla^2\chi = \eta, \qquad \ell_\mu = \sqrt{\frac{3\gamma\ell}{\epsilon_\mu}}, \qquad (30)$$

with ℓ_μ as a characteristic length-scale associated with the micromorphic regularization. Eq. (30) is supplemented by the homogeneous Neumann boundary condition $\nabla\chi \cdot \mathbf{n} = 0$ on the boundary ∂B, which implies $\int_B\chi\mathrm{d}V = \int_B\eta\mathrm{d}V$. The Helmholz-type PDE (30) results in a natural way from the micromorphic approach (Forest, 2009; Forest, 2016). It also appears in other contexts in which it is postulated directly, e.g., in implicit-gradient damage models (Peerlings et al., 1996), softening plasticity (Engelen et al., 2003), and gradient-enhanced crystal plasticity (Stupkiewicz and Petryk, 2016).

Eq. (30) indicates that the term $\epsilon_\mu(\eta - \chi)$ in Eq. (25) is equal to and thus can be substituted by $-3\gamma\ell\nabla^2\chi$. Given that ϵ_μ is adequately large (so that $\nabla\eta \approx \nabla\chi$), the incremental governing equation for η in the original phase-field model, Eq. (19), is then recovered.

3. A finite-deformation phase-field model for multiphase systems

The prototype phase-field model presented in Section 2 is extended here, within the finite-deformation framework, to a system with $N + 1$ phases. A conventional model is presented in Section 3.1, and its micromorphic version is then introduced in Section 3.2. In Section 3.3, the dissipation potential is extended to incorporate both viscous and rate-independent dissipation contributions.

3.1. Conventional phase-field model

In this section, we briefly summarize the model developed recently by Rezaee-Hajidehi and Stupkiewicz (2020). The model possesses $N + 1$ order parameters η_i, representing the austenite

and N variants of martensite. The following inequality and sum-to-unity constraints are imposed on the order parameters,

$$0 \leqslant \eta_i \ (i = 0, \ldots, N) \qquad \text{and} \qquad \sum_{i=0}^{N} \eta_i = 1. \tag{31}$$

The kinematic description is based on the multiplicative split of the deformation gradient $\mathbf{F}$ into the elastic part $\mathbf{F}^e$ and the transformation part $\mathbf{F}^t$,

$$\mathbf{F} = \mathbf{F}^e \mathbf{F}^t, \qquad \mathbf{F} = \nabla \boldsymbol{\varphi} = \mathbf{I} + \nabla \mathbf{u}, \tag{32}$$

where ∇ represents the spatial gradient with respect to the reference configuration, $\boldsymbol{\varphi}$ represents the deformation mapping from the reference to the current configuration, and $\mathbf{I}$ is the second-order identity tensor. The transformation part $\mathbf{F}^t$ is defined as a linear combination of the transformation stretch (Bain) tensors $\mathbf{U}_i^t$,

$$\mathbf{F}^t(\boldsymbol{\eta}) = \sum_{i=0}^{N} \eta_i \mathbf{U}_i^t, \qquad \boldsymbol{\eta} = \{\eta_0, \eta_1, \ldots, \eta_N\}, \tag{33}$$

where $\mathbf{U}_i^t$ are calculated from the crystallographic lattice parameters. We assume the undeformed austenite as the reference state, thus $\mathbf{F}^t = \mathbf{U}_0^t = \mathbf{I}$ for a pure austenitic state, i.e. for $\eta_0 = 1$.

In analogy to Eq. (2), the Helmholtz free energy function is now defined as

$$F(\mathbf{F}, \boldsymbol{\eta}, \nabla \boldsymbol{\eta}) = F_{\text{chem}}(\boldsymbol{\eta}) + F_{\text{el}}(\mathbf{F}, \boldsymbol{\eta}) + F_{\text{int}}(\boldsymbol{\eta}, \nabla \boldsymbol{\eta}). \tag{34}$$

The chemical energy contribution in Eq. (34) is defined as a weighted sum of the chemical energy of the pure phases F_i^0, i.e.

$$F_{\text{chem}}(\boldsymbol{\eta}) = \sum_{i=0}^{N} \eta_i F_i^0. \tag{35}$$

The elastic strain energy F_{el} is expressed as a quadratic function of the Hencky (logarithmic) strain $\mathbf{H}^e = \frac{1}{2} \log \mathbf{C}^e$, where $\mathbf{C}^e = (\mathbf{F}^e)^{\mathsf{T}} \mathbf{F}^e$ is the elastic right Cauchy-Green tensor and $\mathbf{F}^e = \mathbf{F}(\mathbf{F}^t)^{-1}$,

$$F_{\text{el}}(\mathbf{F}, \boldsymbol{\eta}) = \frac{1}{2} (\det \mathbf{F}^t) \mathbf{H}^e \cdot \mathbb{L}(\boldsymbol{\eta}) \mathbf{H}^e, \qquad \mathbb{L}(\boldsymbol{\eta}) = \sum_{i=0}^{N} \eta_i \mathbb{L}_i, \tag{36}$$

with $\mathbb{L}_i$ as the fourth-order elastic stiffness tensor of the phase i.

The interfacial energy F_{int} is employed here in the form of the so-called double-obstacle potential (Steinbach, 2009),

$$F_{\text{int}}(\boldsymbol{\eta}, \nabla \boldsymbol{\eta}) = \sum_{i=0}^{N} \sum_{j=i+1}^{N} \frac{4\gamma_{ij}}{\pi \ell_{ij}} \left(\eta_i \eta_j - \ell_{ij}^2 \nabla \eta_i \cdot \nabla \eta_j \right), \tag{37}$$

where γ_{ij} and ℓ_{ij} denote, respectively, the interfacial energy density and the interface thickness parameter associated with the diffuse interface between the phases i and j.

The viscous-type dissipation potential is adopted in the following form,

$$D(\dot{\boldsymbol{\eta}}) = D^{\text{v}}(\dot{\boldsymbol{\eta}}) = \sum_{i=0}^{N} \frac{\dot{\eta}_i^2}{2m_i}, \tag{38}$$

with m_i as the mobility parameter associated with the phase i. The effective mobility of the interface separating the phases i and j is equal to $m_{ij} = m_i m_j / (m_i + m_j)$ (Rezaee-Hajidehi and Stupkiewicz, 2020).

The evolution problem is formulated next by following the variational framework described in Section 2. Here, we only present the incremental form of the evolution problem. In analogy to Eq. (14), the global incremental potential is defined as

$$\Pi_\tau[\boldsymbol{\varphi}, \boldsymbol{\eta}] = \mathcal{E}[\boldsymbol{\varphi}, \boldsymbol{\eta}] - \mathcal{E}[\boldsymbol{\varphi}_n, \boldsymbol{\eta}_n] + \mathcal{D}_\tau[\boldsymbol{\eta}], \tag{39}$$

where the potential energy functional $\mathcal{E}$ is specified as

$$\mathcal{E}[\boldsymbol{\varphi}, \boldsymbol{\eta}] = \mathcal{F}[\boldsymbol{\varphi}, \boldsymbol{\eta}] + \Omega[\boldsymbol{\varphi}], \qquad \mathcal{F}[\boldsymbol{\varphi}, \boldsymbol{\eta}] = \int_B F(\nabla \boldsymbol{\varphi}, \boldsymbol{\eta}, \nabla \boldsymbol{\eta}) \, \mathrm{d}V, \tag{40}$$

and the global incremental dissipation potential $\mathcal{D}_\tau$ takes the form

$$\mathcal{D}_\tau[\boldsymbol{\eta}] = \int_B D_\tau(\boldsymbol{\eta}) \, \mathrm{d}V,$$

$$D_\tau(\boldsymbol{\eta}) = \tau D\left(\frac{\boldsymbol{\eta} - \boldsymbol{\eta}_n}{\tau}\right) = \sum_{i=0}^{N} \frac{\tau}{2m_i} \left(\frac{\eta_i - \eta_{i,n}}{\tau}\right)^2. \tag{41}$$

Consequently, the evolution problem is formulated as the minimization of the constrained global incremental potential Π_τ^Δ with respect to the fields $\boldsymbol{\varphi}$ and $\boldsymbol{\eta}$, viz.

$$\{\boldsymbol{\varphi}, \boldsymbol{\eta}\} = \arg \min_{\boldsymbol{\varphi}, \boldsymbol{\eta}} \ \Pi_\tau^\Delta[\boldsymbol{\varphi}, \boldsymbol{\eta}], \qquad \Pi_\tau^\Delta[\boldsymbol{\varphi}, \boldsymbol{\eta}] = \Pi_\tau[\boldsymbol{\varphi}, \boldsymbol{\eta}] + \mathcal{I}_\Delta[\boldsymbol{\eta}], \tag{42}$$

where the functional $\mathcal{I}_\Delta$ imposes the physical constraints on the order parameters, see Eq. (31),

$$\mathcal{I}_\Delta[\boldsymbol{\eta}] = \int_B I_\Delta(\boldsymbol{\eta}) \, \mathrm{d}V, \qquad I_\Delta(\boldsymbol{\eta}) = \begin{cases} 0 & \boldsymbol{\eta} \in \Delta^N, \\ +\infty & \text{otherwise}. \end{cases} \tag{43}$$

and I_Δ is the indicator function of the admissible set Δ^N (N-simplex),

$$\Delta^N = \left\{ \boldsymbol{\eta} \in \mathcal{R}^{N+1} : \ 0 \leqslant \eta_i, \ \sum_{i=0}^{N} \eta_i = 1 \right\}. \tag{44}$$

In the computer implementation, the inequality constraints introduced here through $\mathcal{I}_\Delta$ are regularized using the penalty method, see Section 4.1.

3.2. Micromorphic regularization

Following the general scheme presented in Section 2.3, a micromorphic extension of the model presented above will now be developed. Micromorphic variables $\boldsymbol{\chi} = \{\chi_0, \chi_1, \ldots, \chi_N\}$ are thus introduced, which are one-by-one coupled to the order parameters $\boldsymbol{\eta} = \{\eta_0, \eta_1, \ldots, \eta_N\}$. Accordingly, the Helmholtz free energy in Eq. (34) is modified as

$$F(\mathbf{F}, \boldsymbol{\eta}, \boldsymbol{\chi}, \nabla \boldsymbol{\chi}) = F_{\text{chem}}(\boldsymbol{\eta}) + F_{\text{el}}(\mathbf{F}, \boldsymbol{\eta}) + F_{\text{int}}(\boldsymbol{\eta}, \nabla \boldsymbol{\chi}) + F_\mu(\boldsymbol{\eta}, \boldsymbol{\chi}). \tag{45}$$

With reference to Eq. (21), the micromorphic energy term F_μ is adopted in the following form

$$F_\mu(\boldsymbol{\eta}, \boldsymbol{\chi}) = \sum_{i=0}^{N} \frac{1}{2} \epsilon_{\mu,i} (\eta_i - \chi_i)^2, \tag{46}$$

where parameter $\epsilon_{\mu,i}$ is assigned to penalize the difference between η_i and χ_i.

With this modification, the incremental energy minimization problem analogous to that in Eq. (42) can now be formulated. This is omitted here for brevity. As discussed in Section 2.3, upon the micromorphic regularization, the order parameters $\boldsymbol{\eta}$ are treated as local quantities and are solved through a local minimization problem. We thus introduce the local incremental potential π_τ,

$$\pi_\tau(\mathbf{F}, \boldsymbol{\eta}, \boldsymbol{\chi}, \nabla \boldsymbol{\chi}) = F(\mathbf{F}, \boldsymbol{\eta}, \boldsymbol{\chi}, \nabla \boldsymbol{\chi}) - F(\mathbf{F}_n, \boldsymbol{\eta}_n, \boldsymbol{\chi}_n, \nabla \boldsymbol{\chi}_n) + D_\tau(\boldsymbol{\eta}). \tag{47}$$

In order to account for the physical constraints on the order parameters $\boldsymbol{\eta}$, the indicator function I_Δ is added to the local potential π_τ thus yielding the local constrained incremental potential π_τ^Δ,

$$\pi_\tau^\Delta(\mathbf{F}, \boldsymbol{\eta}, \boldsymbol{\chi}, \nabla \boldsymbol{\chi}) = \pi_\tau(\mathbf{F}, \boldsymbol{\eta}, \boldsymbol{\chi}, \nabla \boldsymbol{\chi}) + I_\Delta(\boldsymbol{\eta}). \tag{48}$$

For given $\mathbf{F}, \boldsymbol{\chi}$ and $\nabla \boldsymbol{\chi}$, the following local constrained minimization problem is solved for the local order parameters $\boldsymbol{\eta}$,

$$\boldsymbol{\eta} = \arg\min_{\boldsymbol{\eta}} \ \pi_\tau^{\Delta}(\mathbf{F}, \boldsymbol{\eta}, \boldsymbol{\chi}, \nabla\boldsymbol{\chi}), \tag{49}$$

which leads to the local reduced potential $\pi_\tau^{\Delta,\mathrm{red}}$,

$$\pi_\tau^{\Delta,\mathrm{red}}(\mathbf{F}, \boldsymbol{\chi}, \nabla\boldsymbol{\chi}) = \min_{\boldsymbol{\eta}} \ \pi_\tau^{\Delta}(\mathbf{F}, \boldsymbol{\eta}, \boldsymbol{\chi}, \nabla\boldsymbol{\chi}). \tag{50}$$

Consequently, the global evolution problem is governed by the minimization of the global reduced potential $\Pi_\tau^{\Delta,\mathrm{red}}$ with respect to the fields of $\boldsymbol{\varphi}$ and $\boldsymbol{\chi}$,

$$\{\boldsymbol{\varphi}, \boldsymbol{\chi}\} = \arg\min_{\boldsymbol{\varphi},\boldsymbol{\chi}} \ \Pi_\tau^{\Delta,\mathrm{red}}[\boldsymbol{\varphi}, \boldsymbol{\chi}], \tag{51}$$

where

$$\Pi_\tau^{\Delta,\mathrm{red}}[\boldsymbol{\varphi}, \boldsymbol{\chi}] = \int_B \pi_\tau^{\Delta,\mathrm{red}}(\nabla\boldsymbol{\varphi}, \boldsymbol{\chi}, \nabla\boldsymbol{\chi})\,\mathrm{d}V + \Delta\Omega[\boldsymbol{\varphi}]. \tag{52}$$

As before, stationarity of $\Pi_\tau^{\Delta,\mathrm{red}}$ with respect to $\boldsymbol{\varphi}$ implies mechanical equilibrium and stationarity with respect to $\boldsymbol{\chi}$ results in a PDE that links the micromorphic variables $\boldsymbol{\chi}$ with the local order parameters $\boldsymbol{\eta}$, Eq. (30).

3.3. Inclusion of rate-independent dissipation

Up to now, only the viscous dissipation has been considered. Here, we extend the model to account for the rate-independent dissipation effects. The corresponding mixed-type dissipation potential reads

$$D(\dot{\boldsymbol{\eta}}) = D^{\mathrm{v}}(\dot{\boldsymbol{\eta}}) + D^{\mathrm{in}}(\dot{\boldsymbol{\eta}}), \tag{53}$$

where D^{v} represents the viscous contribution and takes the form (38), while the rate-independent contribution D^{in} is defined as

$$D^{\mathrm{in}}(\dot{\boldsymbol{\eta}}) = \|\dot{\boldsymbol{\eta}}\|_{\mathbf{D}} = \sqrt{\dot{\boldsymbol{\eta}} \cdot \mathbf{D}\dot{\boldsymbol{\eta}}}, \qquad \mathbf{D} = \mathrm{diag}(\kappa_0^2, \kappa_1^2, \ldots, \kappa_N^2). \tag{54}$$

In Eq. (54), $\|\dot{\boldsymbol{\eta}}\|_{\mathbf{D}}$ represents the elliptic norm of $\dot{\boldsymbol{\eta}}$ with respect to $\mathbf{D}$, a symmetric positive-definite matrix composed of the material parameters $\kappa_i > 0$, where κ_i characterizes the rate-independent threshold for the driving force associated with the order parameter η_i. Considering an interface between the phases i and j, while no other phases coexist, the rate-independent dissipation takes the form $D^{\mathrm{in}} = \kappa_{ij}|\dot{\eta}_i|$, in view of $\eta_i = 1 - \eta_j$ and thus $\dot{\eta}_i = -\dot{\eta}_j$, where the effective rate-independent threshold κ_{ij} is equal to $\kappa_{ij} = \sqrt{\kappa_i^2 + \kappa_j^2}$.

In the case of the viscous dissipation, the transformation is triggered by a vanishingly small driving force, see the related classical Ginzburg–Landau equation (1). The mixed-type dissipation of the form (53) introduces a rate-independent threshold on the driving force that must be overcome to trigger the transformation. Once the threshold is exceeded, the response is rate dependent (in some sense, similar to the Perzyna-type overstress viscoplasticity).

Upon time-discretization, the mixed-type dissipation potential is transformed to

$$D_\tau(\boldsymbol{\eta}) = D_\tau^{\mathrm{v}}(\boldsymbol{\eta}) + D_\tau^{\mathrm{in}}(\boldsymbol{\eta}), \qquad D_\tau^{\mathrm{in}}(\boldsymbol{\eta}) = \|\Delta\boldsymbol{\eta}\|_{\mathbf{D}} = \sqrt{\Delta\boldsymbol{\eta} \cdot \mathbf{D}\Delta\boldsymbol{\eta}}, \tag{55}$$

where the viscous part D_τ^{v} takes the form as in Eq. $(41)_2$ and $\Delta\boldsymbol{\eta} = \boldsymbol{\eta} - \boldsymbol{\eta}_n$.

The incremental dissipation potential D_τ of the form (55) can now be used instead of the viscous dissipation potential $(41)_2$ in the global minimization problem (42) of the conventional phase-field model and in the local minimization problem (49) of the micromorphic model, while the general structure of the incremental energy minimization framework remains intact. However, inclusion of the rate-independent dissipation renders the minimization problems (42) and (49) non-smooth, due to the

non-differentiability of D_τ^{in} at $\Delta\boldsymbol{\eta} = \mathbf{0}$. To address this issue, the augmented Lagrangian technique is employed in this work, see Section 4.2.

A phase-field model with a mixed-type dissipation of the general form (53) has been developed by Tůma et al., 2018 for the case of two phases (one order parameter). The dissipation potential (53)–(54) is an extension of that model to the case of multivariant transformation. While the extension itself is straightforward, its computational treatment is by far more involved. In particular, as shown later, the micromorphic formulation of the phase-field model is highly beneficial when it comes to computer implementation.

4. Finite-element implementation

The two main issues in the finite-element implementation of the presented models are the enforcement of the inequality constraints on the order parameters and the treatment of the non-smooth minimization as a result of including the rate-independent dissipation. These are addressed here by employing, respectively, the standard penalty regularization (Section 4.1) and the augmented Lagrangian technique (Section 4.2). For conciseness, the respective details are presented for the micromorphic model only, since the respective formulations for the conventional phase-field model follow a similar procedure. The solution procedure and the computer implementation in the finite-element method are commented in Sections 4.3 and 4.4, respectively.

4.1. Penalty regularization

In the computer implementation, the order parameter η_0 corresponding to the austenite phase is considered as a dependent variable. In view of the sum-to-unity constraint, Eq. $(31)_2$, η_0 is simply defined as a function of the other order parameters, i.e.

$$\eta_0 = \eta_0(\hat{\boldsymbol{\eta}}) = 1 - \sum_{i=1}^{N} \eta_i, \qquad \boldsymbol{\eta} = \boldsymbol{\eta}(\hat{\boldsymbol{\eta}}), \qquad \hat{\boldsymbol{\eta}} = \{\eta_1, \ldots, \eta_N\}, \tag{56}$$

with $\hat{\boldsymbol{\eta}}$ denoting the vector of condensed order parameters. In a similar way, the micromorphic variable χ_0 is defined as $\chi_0 = \chi_0(\hat{\boldsymbol{\chi}}) = 1 - \sum_{i=1}^{N} \chi_i$ and thus $\boldsymbol{\chi} = \boldsymbol{\chi}(\hat{\boldsymbol{\chi}})$, where $\hat{\boldsymbol{\chi}} = \{\chi_1, \ldots, \chi_N\}$. Accordingly, the local incremental potential, Eq. (47), is expressed in terms of the condensed variables $\hat{\boldsymbol{\eta}}$ and $\hat{\boldsymbol{\chi}}$ as

$$\hat{\pi}_\tau(\mathbf{F}, \hat{\boldsymbol{\eta}}, \hat{\boldsymbol{\chi}}, \nabla\hat{\boldsymbol{\chi}}) = \pi_\tau(\mathbf{F}, \boldsymbol{\eta}(\hat{\boldsymbol{\eta}}), \boldsymbol{\chi}(\hat{\boldsymbol{\chi}}), \nabla\boldsymbol{\chi}(\nabla\hat{\boldsymbol{\chi}})). \tag{57}$$

The penalty regularization of the inequality constraints $\eta_i \geqslant 0$ is now performed by replacing the indicator function I_Δ in the incremental potential π_τ^{Δ}, see Eq. (48), by the respective penalty term I_Δ^{pen},

$$I_\Delta^{\mathrm{pen}} = \sum_{i=0}^{N} \frac{1}{2}\epsilon_\eta \langle \eta_i \rangle_{-}^2, \tag{58}$$

thus yielding the regularized potential $\hat{\pi}_\tau^{\mathrm{pen}}$,

$$\hat{\pi}_\tau^{\mathrm{pen}}(\mathbf{F}, \hat{\boldsymbol{\eta}}, \hat{\boldsymbol{\chi}}, \nabla\hat{\boldsymbol{\chi}}) = \hat{\pi}_\tau(\mathbf{F}, \hat{\boldsymbol{\eta}}, \hat{\boldsymbol{\chi}}, \nabla\hat{\boldsymbol{\chi}}) + I_\Delta^{\mathrm{pen}}(\hat{\boldsymbol{\eta}}). \tag{59}$$

Here ϵ_η is the penalty regularization parameter, and the angular bracket $\langle x \rangle_{-}$ returns only the negative value of x, i.e. $\langle x \rangle_{-} = (x - |x|)/2$. The constrained minimization problem (49) is thus transformed into an unconstrained problem,

$$\hat{\boldsymbol{\eta}} = \arg\min_{\hat{\boldsymbol{\eta}}} \ \hat{\pi}_\tau^{\mathrm{pen}}(\mathbf{F}, \hat{\boldsymbol{\eta}}, \hat{\boldsymbol{\chi}}, \nabla\hat{\boldsymbol{\chi}}). \tag{60}$$

The subsequent steps of the incremental energy minimization scheme, in particular the minimization of the reduced global potential, Eq. (51), are then executed as described in Section 3.2,

except that the micromorphic variables $\boldsymbol{\chi}$ are replaced by the condensed variables $\hat{\boldsymbol{\chi}}$.

The results reported recently for 2D problems (Rezaee-Hajidehi and Stupkiewicz, 2020) and for large-scale 3D problems (Tůma et al., 2021), the latter obtained using an iterative multigrid solver, indicate that the penalty method performs reasonably well in combination with the double-obstacle potential. Specifically, the computational efficiency is not seriously affected for sufficiently large values of the penalty parameter ϵ_η that result in an insignificant violation of the inequality constraints $\eta_i \geqslant 0$.

4.2. Augmented Lagrangian technique

When the mixed-type dissipation is considered, the minimization problem (60) is non-smooth and therefore requires a special treatment on account of the rate-independent dissipation term D_τ^{in}, see Eq. (55), in the incremental potential π_τ, see Eqs. (47) and (57). The augmented Lagrangian technique has been employed in this work as an efficient computational tool that transforms the non-smooth minimization problem (60) to an equivalent smooth saddle-point problem. To this end, a set of Lagrange multipliers $\hat{\boldsymbol{\lambda}} = \{\hat{\lambda}_1, \ldots, \hat{\lambda}_N\}$ is introduced and the following Lagrange function is formulated,

$$\mathcal{L}\left(\mathbf{F}, \hat{\boldsymbol{\eta}}, \hat{\boldsymbol{\chi}}, \nabla\hat{\boldsymbol{\chi}}, \hat{\boldsymbol{\lambda}}\right) = \widehat{F}(\mathbf{F}, \hat{\boldsymbol{\eta}}, \hat{\boldsymbol{\chi}}, \nabla\hat{\boldsymbol{\chi}}) + \widehat{D}_\tau^{\mathrm{v}}(\hat{\boldsymbol{\eta}}) + L^{\mathrm{in}}\left(\hat{\boldsymbol{\eta}}, \hat{\boldsymbol{\lambda}}\right) + I_\Delta^{\mathrm{pen}}(\hat{\boldsymbol{\eta}}),$$

(61)

in which the non-differentiable rate-independent dissipation term $\widehat{D}_\tau^{\mathrm{in}}(\hat{\boldsymbol{\eta}}) = D_\tau^{\mathrm{in}}(\boldsymbol{\eta}(\hat{\boldsymbol{\eta}}))$ in the incremental potential $\hat{\pi}_\tau$, see Eqs. (47), (55) and (57), has been replaced by a continuously differentiable function L^{in}, see Appendix A,

$$L^{\mathrm{in}}(\hat{\boldsymbol{\eta}}, \hat{\boldsymbol{\lambda}}) = \begin{cases} \left(\hat{\boldsymbol{\lambda}} + \frac{1}{2}\varrho\mathbf{D}\Delta\hat{\boldsymbol{\eta}}\right) \cdot \Delta\hat{\boldsymbol{\eta}} & \text{if } \|\hat{\boldsymbol{\lambda}}_{\mathrm{aug}}\|_{\mathbf{D}^{-1}} \leqslant 1, \\ -\frac{1}{2\varrho}\left(\|\hat{\boldsymbol{\lambda}}\|_{\mathbf{D}^{-1}}^2 - 2\|\hat{\boldsymbol{\lambda}}_{\mathrm{aug}}\|_{\mathbf{D}^{-1}} + 1\right) & \text{otherwise,} \end{cases}$$

(62)

where $\hat{\boldsymbol{\lambda}}_{\mathrm{aug}} = \hat{\boldsymbol{\lambda}} + \varrho\mathbf{D}\Delta\hat{\boldsymbol{\eta}}$ is the vector of augmented Lagrange multipliers and $\varrho > 0$ is a regularization parameter. Functions $\widehat{F}$ and $\widehat{D}_\tau^{\mathrm{v}}$ in Eq. (61) correspond to the respective functions F and D_τ^{v} with the arguments $\boldsymbol{\eta}$ and $\boldsymbol{\chi}$ replaced by their condensed counterparts $\hat{\boldsymbol{\eta}}$ and $\hat{\boldsymbol{\chi}}$, as in Eq. (57). Note that the constant term representing the free energy at the previous time step has been discarded in Eq. (61).

The solution of the local problem is now obtained by solving the following smooth and unconstrained saddle-point problem,

$$\{\hat{\boldsymbol{\eta}}, \hat{\boldsymbol{\lambda}}\} = \arg\min_{\hat{\boldsymbol{\eta}}} \max_{\hat{\boldsymbol{\lambda}}} \mathcal{L}\left(\mathbf{F}, \hat{\boldsymbol{\eta}}, \hat{\boldsymbol{\chi}}, \nabla\hat{\boldsymbol{\chi}}, \hat{\boldsymbol{\lambda}}\right).$$

(63)

Considering that the Lagrangian $\mathcal{L}$ is continuously differentiable, the solution can be obtained by directly solving the stationarity conditions, see Eq. (A.13), using the Newton method.

The condition of stationarity of $\mathcal{L}$ with respect to $\hat{\boldsymbol{\eta}}$ and $\hat{\lambda}$ can be written in the following form,

$$\mathbf{Q}_g(\mathbf{E}_g, \mathbf{h}_g) = \mathbf{0}, \qquad \mathbf{Q}_g(\mathbf{E}_g, \mathbf{h}_g) = \frac{\partial\tilde{\mathcal{L}}(\mathbf{E}_g, \mathbf{h}_g)}{\partial\mathbf{h}_g},$$

(64)

where the local unknowns have been gathered in the vector $\mathbf{h}_g = \{\hat{\boldsymbol{\eta}}_g, \hat{\lambda}_g\}$, and the local independent variables in the vector $\mathbf{E}_g = \{\mathbf{F}_g, \hat{\boldsymbol{\chi}}_g, \nabla\hat{\boldsymbol{\chi}}_g\}$, so that $\mathcal{L} = \tilde{\mathcal{L}}(\mathbf{E}_g, \mathbf{h}_g)$. Here, anticipating that in the finite-element setting the local problem will be solved at element Gauss points, the subscript g has been added as the Gauss-point index.

The stationarity condition (64) is then solved using the Newton method,

$$\Delta\mathbf{h}_g^j = -\left(\frac{\partial\mathbf{Q}_g}{\partial\mathbf{h}_g}\right)^{-1}\mathbf{Q}_g\left(\mathbf{E}_g, \mathbf{h}_g^j\right), \qquad \mathbf{h}_g^{j+1} = \mathbf{h}_g^j + \Delta\mathbf{h}_g^j,$$

(65)

where $\partial\mathbf{Q}_g/\partial\mathbf{h}_g$ is the local tangent matrix and the iterative scheme (with j denoting the iteration number) is repeated until convergence is obtained. Recall that the Lagrangian $\mathcal{L}$ is continuously differentiable and hence the residual $\mathbf{Q}_g$ is a continuous function of $\mathbf{h}_g$.

The solution $\mathbf{h}_g$ depends on the independent variables $\mathbf{E}_g$, i.e. $\mathbf{h}_g = \mathbf{h}_g(\mathbf{E}_g)$, and the derivative of this implicit dependence is needed to compute the global tangent matrix, see Section 4.3. This derivative is obtained by taking the total derivative of the local residual $\mathbf{Q}_g(\mathbf{E}_g, \mathbf{h}_g(\mathbf{E}_g)) = \mathbf{0}$, Eq. (64), with respect to $\mathbf{E}_g$, which leads to (Michaleris et al., 1994; Korelc, 2009)

$$\frac{\partial\mathbf{h}_g}{\partial\mathbf{E}_g} = -\left(\frac{\partial\mathbf{Q}_g}{\partial\mathbf{h}_g}\right)^{-1}\frac{\partial\mathbf{Q}_g}{\partial\mathbf{E}_g}.$$

(66)

It can be checked that $\nabla\hat{\boldsymbol{\chi}}_g$ does not appear in the stationarity condition (64), see Eq. (25) of the prototype model in Section 2.3, so that the solution $\mathbf{h}_g$ does not depend on $\nabla\hat{\boldsymbol{\chi}}_g$. Accordingly, $\nabla\hat{\boldsymbol{\chi}}_g$ is only formally included in $\mathbf{E}_g$.

The beneficial feature of the augmented Lagrangian method is that the solution of the saddle-point problem (63) does not depend on the regularization parameter ϱ. The value of ϱ may affect the convergence of the iterative Newton scheme (65), however, in practice there is quite some freedom in choosing ϱ with no considerable impact on the performance of the computational scheme. Such behaviour has been observed for the micromorphic formulation in which the saddle-point problem is solved locally at each Gauss point. For instance, in the case of one order parameter, the value of ϱ can be safely varied by several orders of magnitude. On the other hand, in the case of the conventional formulation in which the saddle-point problem is solved at the global level, see Section 4.3.2, ϱ turns out to have a narrower range of suitable values.

Function L^{in} in Eq. (62) has been derived in Appendix A by generalizing the augmented Lagrangian treatment of the pure friction problem following Alart and Curnier (1991), see also Pietrzak and Curnier (1999). In a scalar case, which would correspond here to a single order parameter, a similar approach has been employed by Stupkiewicz and Petryk (2013) in the macroscopic model of pseudoelasticity, where a single Lagrange multiplier has been used to handle both the rate-independent dissipation and the bound constraints on the martensite volume fraction, see also Tůma et al. (2018) for the application of the method in a phase-field model with the mixed-type dissipation. A generalization of this approach to the case of multiple order parameters is not available, and for this reason the inequality constraints in the present work are regularized using the penalty method.

4.3. Finite-element discretization and solution procedure

The simulations are carried out in this work for two formulations (conventional and micromorphic) and for two types of dissipation (viscous and mixed-type), which gives the total of four different models. The finite-element discretization and the related solution procedure are briefly described below for the most complex case of the micromorphic phase-field model with the mixed-type dissipation. The remaining models are then commented by pointing out the differences with respect to this case.

4.3.1. Micromorphic model with the mixed-type dissipation

In the micromorphic formulation, the finite-element approximation is introduced for the global fields $\boldsymbol{\varphi}$ and $\hat{\boldsymbol{\chi}}$, namely

$$\boldsymbol{\varphi}^h = \sum_i \mathbf{N}_i^{(\varphi)} \boldsymbol{\varphi}_i, \qquad \hat{\boldsymbol{\chi}}^h = \sum_i \mathbf{N}_i^{(\chi)} \hat{\boldsymbol{\chi}}_i, \tag{67}$$

where $\boldsymbol{\varphi}_i$ and $\hat{\boldsymbol{\chi}}_i$ are the nodal quantities and $\mathbf{N}_i^{(\varphi)}$ and $\mathbf{N}_i^{(\chi)}$ are the corresponding basis functions. The global incremental potential $\Pi_\tau^{\Delta,\text{red}}$, Eq. (52), is then evaluated in terms of the discretized fields $\boldsymbol{\varphi}^h$ and $\boldsymbol{\chi}^h = \boldsymbol{\chi}^h(\hat{\boldsymbol{\chi}}^h)$, which leads to the following discrete incremental potential,

$$\Pi_\tau^h(\mathbf{p}, \mathbf{h}) = \Pi_\tau^{\Delta,\text{red}}[\boldsymbol{\varphi}^h, \boldsymbol{\chi}^h], \tag{68}$$

where $\mathbf{p} = \{\mathbf{p_u}, \mathbf{p_\chi}\}$ is the global vector of unknowns with $\mathbf{p_u}$ denoting the global vector of nodal displacements $\mathbf{u}_i = \boldsymbol{\varphi}_i - \mathbf{X}_i$ and $\mathbf{p_\chi}$ denoting the global vector of nodal micromorphic variables $\hat{\boldsymbol{\chi}}_i$. Following the standard approach, the discrete potential Π_τ^h is evaluated by performing a numerical integration (Gauss quadrature) over individual finite elements.

In Eq. (68), it is indicated that the discrete potential Π_τ^h depends also on the vector $\mathbf{h}$ that collects all the local (Gauss-point) variables $\mathbf{h}_g = \{\hat{\boldsymbol{\eta}}_g, \hat{\lambda}_g\}$, see Section 4.2. As described in Section 4.2, the local variables implicitly depend on the global variables $\mathbf{p}$, so that we have $\mathbf{h} = \mathbf{h}(\mathbf{p})$ as the global counterpart of the local dependence $\mathbf{h}_g = \mathbf{h}_g(\mathbf{E}_g)$ since we have $\mathbf{E}_g = \mathbf{E}_g(\mathbf{p}_e)$, where $\mathbf{p}_e$ denotes the local vector of nodal unknowns that the Gauss-point variables $\mathbf{E}_g$ depend on (Korelc, 2009).

The discrete potential Π_τ^h is minimized using the Newton method. Stationarity of Π_τ^h with respect to $\mathbf{p}$ yields the global residual,

$$\mathbf{R}(\mathbf{p}, \mathbf{h}(\mathbf{p})) = \mathbf{0}, \qquad \mathbf{R}(\mathbf{p}, \mathbf{h}) = \frac{\partial \Pi_\tau^h(\mathbf{p}, \mathbf{h})}{\partial \mathbf{p}}, \tag{69}$$

which is solved using the following iterative scheme,

$$\Delta \mathbf{p}^k = -\mathbf{K}^{-1} \mathbf{R}(\mathbf{p}^k, \mathbf{h}(\mathbf{p}^k)), \qquad \mathbf{p}^{k+1} = \mathbf{p}^k + \Delta \mathbf{p}^k. \tag{70}$$

In Eq. (70), $\mathbf{K}$ denotes the global tangent matrix,

$$\mathbf{K} = \frac{\partial \mathbf{R}}{\partial \mathbf{p}} + \frac{\partial \mathbf{R}}{\partial \mathbf{h}} \frac{\partial \mathbf{h}}{\partial \mathbf{p}} = \frac{\partial \mathbf{R}}{\partial \mathbf{p}} - \frac{\partial \mathbf{R}}{\partial \mathbf{h}} \left(\frac{\partial \mathbf{Q}}{\partial \mathbf{h}} \right)^{-1} \frac{\partial \mathbf{Q}}{\partial \mathbf{p}}, \tag{71}$$

and the following implicit derivative has been taken into account,

$$\frac{\partial \mathbf{h}}{\partial \mathbf{p}} = -\left(\frac{\partial \mathbf{Q}}{\partial \mathbf{h}} \right)^{-1} \frac{\partial \mathbf{Q}}{\partial \mathbf{p}}. \tag{72}$$

The above expression is obtained as the global counterpart of Eq. (66) formulated here for the global residual $\mathbf{Q}(\mathbf{p}, \mathbf{h}) = \mathbf{0}$.

Concluding, the computational scheme described above leads to a nested iterative-subiterative scheme, similar to that commonly used in the classical elastoplasticity (Michaleris et al., 1994; Korelc, 2009). The lower-level Newton scheme (65), which is solved at the element Gauss points, results from the micromorphic formulation introduced in Section 3.2 and corresponds to the local minimization problem (60) which has been transformed to the saddle-point problem (63) using the augmented Lagrangian method. The upper-level Newton scheme (70) is solved on the global level and corresponds to the minimization (51) of the reduced global potential. The resulting coupled problem involving the displacements and the micromorphic variables is solved in a monolithic manner simultaneously with respect to all global unknowns. Thanks to the micromorphic formulation, the complexity, which is here related to the non-smooth rate-independent dissipation contribution, is shifted to the local problem that can be solved in an efficient and robust manner (here using the the augmented Lagrangian method). Moreover, special techniques, such as line search or substepping, can be additionally used at the Gauss-point level to improve the robustness of the computational scheme. This is facilitated by the micromorphic formulation, while such techniques would be less efficient when applied at the global level in the conventional formulation discussed below.

4.3.2. Conventional model with the mixed-type dissipation

The augmented Lagrangian treatment of the mixed-type dissipation can also be applied in the case of the conventional formulation. The non-smooth minimization problem (42) with the incremental mixed-type dissipation potential (55) is then transformed to a global saddle-point problem similar to that in Eq. (63). Upon the finite-element discretization, the global problem is thus formulated as the condition of stationarity of the corresponding Lagrangian function with respect to the nodal displacements, order parameters and Lagrange multipliers. This is in contrast to the micromorphic formulation in which the Lagrange multipliers are local unknowns. Recall that the number of Lagrange multipliers is equal to the number of (condensed) order parameters. Hence, in the case of a multivariant transformation (with multiple order parameters), the size of the problem increases significantly for the conventional formulation.

According to our experience, the global formulation of the augmented Lagrangian method is also significantly less robust compared to the local one that results from the micromorphic formulation. This manifests itself in a strong sensitivity of the convergence behaviour to the value of the regularization parameter ϱ and severe convergence issues in the case of a multivariant transformation.

Due to the above drawbacks of the conventional formulation, its applications reported in this paper are limited to the case of a single order parameter, see Section 5.2. The corresponding conventional model is similar to that developed by Tůma et al. (2018) for the case of a single order parameter and a single Lagrange multiplier, where the latter was also used to handle the bound constraints on the order parameter ($0 \leqslant \eta \leqslant 1$), see Stupkiewicz and Petryk (2013) for the details of the respective augmented Lagrangian treatment.

4.3.3. Micromorphic model with the viscous dissipation

In the case of the viscous dissipation, the micromorphic formulation leads to a nested iterative-subiterative Newton scheme, as in the case of the mixed-type dissipation, Section 4.3.1. However, this time, the local problem does not require any special treatment and simply amounts to solving nonlinear equations that express the condition of stationarity of the local incremental potential (59) with respect to the local order parameters. At the same time, the global problem is solved with respect to the nodal displacements and micromorphic variables, as outlined in Section 4.3.1.

Note that, in the case of the viscous dissipation, the micromorphic formulation does not bring any benefit with respect to the conventional formulation which is straightforward and the corresponding computational scheme behaves well. This case is thus considered for completeness only.

4.3.4. Conventional model with the viscous dissipation

In this case, the finite-element discretization and the solution procedure are straightforward. Upon the penalty regularization, as described in Section 4.1, the global incremental potential (42) is directly evaluated in terms of the global unknowns representing the nodal displacements and order parameters, and the Newton method is applied to solve the global equations resulting from the respective stationarity condition. The corresponding model is

the same as that introduced in our recent work (Rezaee-Hajidehi and Stupkiewicz, 2020), see also Tůma et al. (2021).

4.4. Details of the finite-element implementation

The spatial discretization of the body domain B is carried out by using the standard four-noded quadrilateral finite elements and the piecewise-bilinear basis functions are employed for all the fields. The global residual vector and the corresponding global tangent matrix required in the Newton method are evaluated and assembled efficiently using the automatic differentiation (AD) technique and the symbolic code generation tool *AceGen* (Korelc and Wriggers, 2016). To perform the finite-element simulations, the resulting computer codes are then incorporated into the finite-element environment *AceFEM*, which is closely interfaced with *AceGen*. An adaptive time-stepping strategy is employed in the simulations in order to adjust the size of the current time step based on the number of Newton iterations needed to converge to the solution at the previous time step. The direct MKL PARDISO solver is employed to solve the linear system of equations at each Newton iteration. All the computations are conducted on a 12-core workstation equipped with Intel i9-10920X CPU and 128 GB RAM.

A closed-form representation of the matrix logarithm along with an exact and computationally efficient derivation of its first and second derivatives are facilitated by *AceGen* (Hudobivnik and Korelc, 2016). On account of this, evaluation of the Hencky strain, see Eq. (36), and its derivatives are done in a straightforward manner.

In the conventional formulation, spurious stresses may develop within the diffuse interfaces due to an inconsistent approximation of the deformation gradient $\mathbf{F} = \nabla\boldsymbol{\varphi}$ and its transformation part $\mathbf{F}^{\mathrm{t}}$. To circumvent this, $\mathbf{F}^{\mathrm{t}}$ is then assumed constant within each element and is evaluated at the center of the element, see Tůma et al. (2016). In the micromorphic formulation, such an inconsistency is much weaker and the related treatment is not needed.

In the numerical studies presented in Section 5, the external load (indentation) is exerted on the body through a frictionless contact interaction with a rigid circular indenter. The contact constraint, i.e. the impenetrability condition, is enforced by using the standard penalty method (Wriggers, 2006).

5. Illustrative numerical examples

5.1. Problem setup

In this section, we report the results of numerical studies carried out using the micromorphic phase-field model presented in Section 3.2. Microstructure evolution during nano-indentation has been chosen as a model problem. The first study concerns the computational efficiency of the micromorphic model as compared to the conventional one. For this purpose, the computational performance is tested for a simple system with two phases (austenite and a single variant of martensite). In the second study, we consider the problem examined in our recent work (Rezaee-Hajidehi and Stupkiewicz, 2020), where the microstructure evolution and the related pseudoelastic response were studied for a system with 5 phases (austenite and 4 variants of martensite), and show the impact of the rate-independent dissipation contribution on the simulation results. In the last study, we extend the setup of the second example and investigate further the effect of the rate-independent dissipation on the martensite microstructure relaxation and on the subsequent microstructure rearrangement during the indentation loading–unloading cycle.

Fig. 1 depicts the sketch of the 2D plane-strain nano-indentation problem. The simulations are performed for a rectangular computational domain with dimensions $W \times H$ discretized by a uniform mesh of quadrilateral elements of the size h. The loading is applied at the top boundary by the frictionless contact with a rigid circular indenter of the radius R, up to the maximum indentation depth $\delta_{\max}$, followed by the withdrawal of the indenter to its initial position. The displacement of the indenter is prescribed at a constant speed of $v = 5$ nm/s during the loading–unloading cycle. The vertical displacement is constrained at the bottom boundary and the horizontal displacement is constrained at the lateral boundaries. The details of the problem setup are provided in Table 1.

The material parameters adopted in the simulations are as follows (unless stated otherwise). The interfacial energy densities that characterize the austenite–martensite and martensite–martensite interfaces are adopted as $\gamma_{0i} = \gamma_{\mathrm{am}} = 0.4$ J/m^2 and $\gamma_{ij} = \gamma_{\mathrm{mm}} = 0.2$ J/m^2, respectively, see Section 4.1 in Rezaee-Hajidehi and Stupkiewicz (2020) for the discussion regarding the justification of the choice of γ_{am} and γ_{mm}. It is assumed that all austenite–martensite and martensite–martensite diffuse interfaces possess the same theoretical thickness with the thickness parameter $\ell_{ij} = \ell = 4$ nm so that the theoretical equilibrium interface thickness is equal to $\pi\ell \approx 12.5$ nm, see Appendix A in Tůma et al. (2018). In order to maintain the austenite as the stable phase in stress-free conditions, the chemical energy of transformation is taken as $\Delta F^0 = F_{\mathrm{m}}^0 - F_{\mathrm{a}}^0 = 10$ MPa, where $F_0^0 = F_{\mathrm{a}}^0$ and $F_i^0 = F_{\mathrm{m}}^0$ are the respective values for the austenite and for the martensite variants. An anisotropic elastic stiffness tensor of cubic symmetry is considered for all phases, and the elastic constants of a CuAlNi single crystal have been used, i.e. $c_{11} = 142$ GPa, $c_{12} = 126$ GPa and $c_{44} = 96$ GPa (Suezawa and Sumino, 1976). The same mobility parameter is set for all phases, namely $m_i = m = 1$ (MPa s)$^{-1}$. The penalty regularization parameter $\epsilon_\eta = 10^3$ GPa is adopted as a result of the trade-off between the violation of the inequality constraints $\eta_i \geqslant 0$ and the computational efficiency. Finally, the regularization parameter involved in the augmented Lagrangian treatment of the rate-independent dissipation is selected as $\varrho = 100$ GPa.

5.2. Numerical study #1: micromorphic vs. conventional phase-field model

The aim of the first study is to compare the computational performance of the micromorphic phase-field model with the conventional one (in the sequel, referred to as 'μPF' and 'PF', respectively) for a possibly simple problem for which both models perform sat-
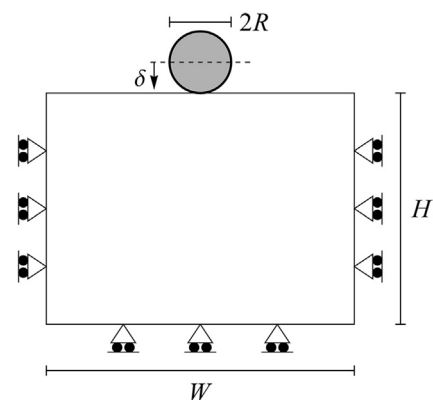

Fig. 1. Geometry and boundary conditions of the 2D nano-indentation problem.

Table 1
Details of the problem setup for different numerical studies.

	$W \times H$ [nm^2]	R [nm]	$\delta_{\max}$ [nm]	h [nm]
Numerical study #1	1500×750	50	50	1.8
Numerical study #2	1000×1000	50	30	1.8
Numerical study #3	1000×1000	150	30	1.5

isfactorily. Accordingly, simulations are carried out using both models for a system with a single order parameter in two scenarios, namely for the purely viscous dissipation and for the mixed-type dissipation. In the case of the viscous dissipation, implementation of the conventional formulation is straightforward, hence there is no need of employing the micromorphic regularization (and no related benefit is expected). The corresponding μPF model is included in this study for completeness and to show that the micromorphic formulation behaves well also in this case. In the case of the mixed-type dissipation, the results reported below clearly highlight the computational benefits delivered by the micromorphic formulation. A comparison of the two formulations for a more general case of several order parameters is not reported here for the reasons explained at the end of this subsection.

In this study, we consider a computational domain of $W \times H = 1500 \times 750$ nm^2, and the element size is $h = 1.8$ nm. The element size has been adopted such that the diffuse interfaces can be properly resolved by the finite-element mesh (recall that the theoretical interface thickness is 12.5 nm). In the actual computations, only one half of the domain is computed, with the proper boundary conditions imposed on the symmetry axis. This results in 168 000 elements and approximately 505 600 degrees of freedom. Note that in the case of the PF model with the mixed-type dissipation, the Lagrange multipliers constitute the global unknowns, in addition to the nodal displacements and order parameters. Accordingly, the corresponding number of degrees of freedom reaches approximately 674 500. The radius of the indenter is selected as $R = 50$ nm and the maximum indentation depth is prescribed as $\delta_{\max} = 50$ nm. For the simulations with the mixed-type dissipation, the rate-independent thresholds are adopted as $\kappa_i = \kappa = 10$ MPa.

The square-to-rectangle martensitic transformation addressed here is described by the following transformation stretch tensor,

$$\mathbf{U}_1^{\mathrm{t}} = \begin{pmatrix} \alpha & 0 \\ 0 & \beta \end{pmatrix}, \tag{73}$$

where the stretch parameters $\alpha = 1.05$ and $\beta = 0.95$ are adopted such that the transformation is associated with a negligible volume change, typical for shape memory alloys. According to the crystallographic theory of martensite (Bhattacharya, 2003), the austenite–martensite interface in this case is oriented at approximately $\pm 45°$.

Fig. 2(a) shows a snapshot of the microstructure evolution (represented by the volume fraction of martensite $\eta = \eta_1$) at the maximum indentation depth $\delta = 50$ nm for the case with the viscous dissipation. It has been observed that the inclusion of the rate-independent dissipation does not cause a qualitatively different microstructure evolution, as only the size of the transformed domain is slightly smaller, and some minor changes are noticeable at the end of the reverse transformation (not shown here). These small differences are also reflected in the indentation load–depth (P–δ) response, Fig. 2(c). In particular, the nucleation event associated with the transformation onset is delayed and a larger hysteresis loop is observed in the case of the mixed-type dissipation.

Before discussing the computational performance, we first evaluate the error induced by the micromorphic regularization. To illustrate this, we consider the case of the purely viscous dissipation and examine the difference between the volume fraction η and its micromorphic counterpart χ at the maximum indentation depth $\delta = 50$ nm for different values of the micromorphic penalty parameter ϵ_μ, namely for $\epsilon_\mu = 1, 2$ and 5 GPa. The corresponding distributions of $\eta - \chi$ are shown in Fig. 3. It follows that within the range of ϵ_μ considered here, the difference between η and χ is not severe, and it is reduced as ϵ_μ is increased. For instance, the maximum value of the absolute difference $|\eta - \chi|$ is obtained equal to 0.11 and 0.03 for $\epsilon_\mu = 1$ GPa and $\epsilon_\mu = 5$ GPa, respectively. Note that the effect of ϵ_μ on the microstructure (the size and shape of the transformed domain) and on the P–δ response has been found to be negligibly small. The corresponding results are thus not provided here.

Fig. 4 summarizes the computational performance of the PF and μPF models, with the latter examined for several values of the micromorphic penalty parameter ϵ_μ. It can be seen that, in the case of the viscous dissipation, Fig. 4(a), the μPF model with moderate

(a)   (b)   (c)
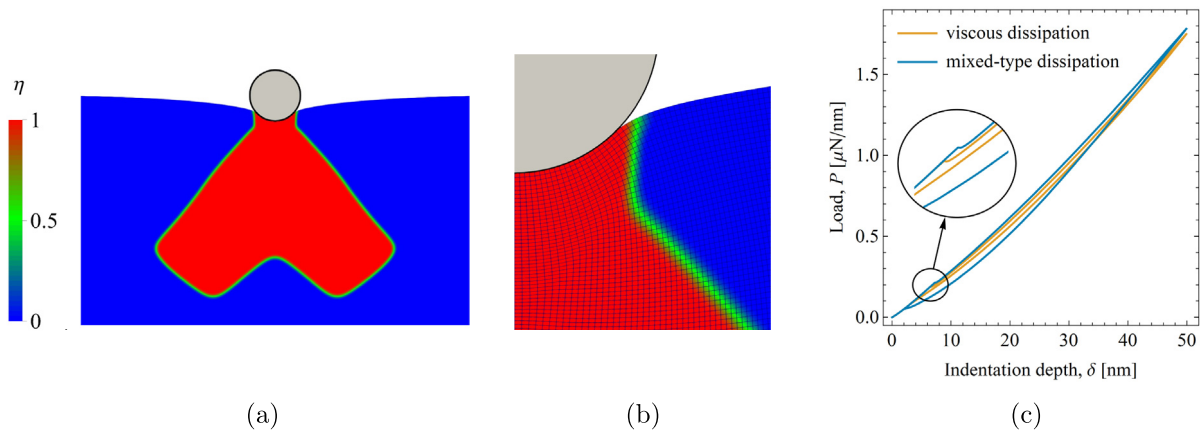
Fig. 2. Numerical study #1: (a) microstructure at the maximum indentation depth $\delta = 50$ nm for the case with the viscous dissipation, (b) a close-up of the deformed mesh and the diffuse interface in the vicinity of the indenter, and (c) the P–δ responses.
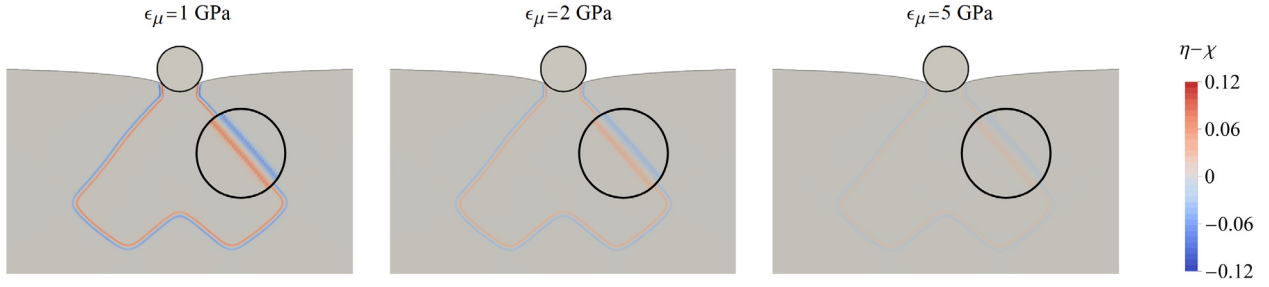
Fig. 3. Numerical study #1: distribution of the difference between η and χ for different values of the micromorphic penalty parameter ϵ_μ (viscous dissipation, $\delta = 50$ nm). The insets show an enlarged view of the interface.
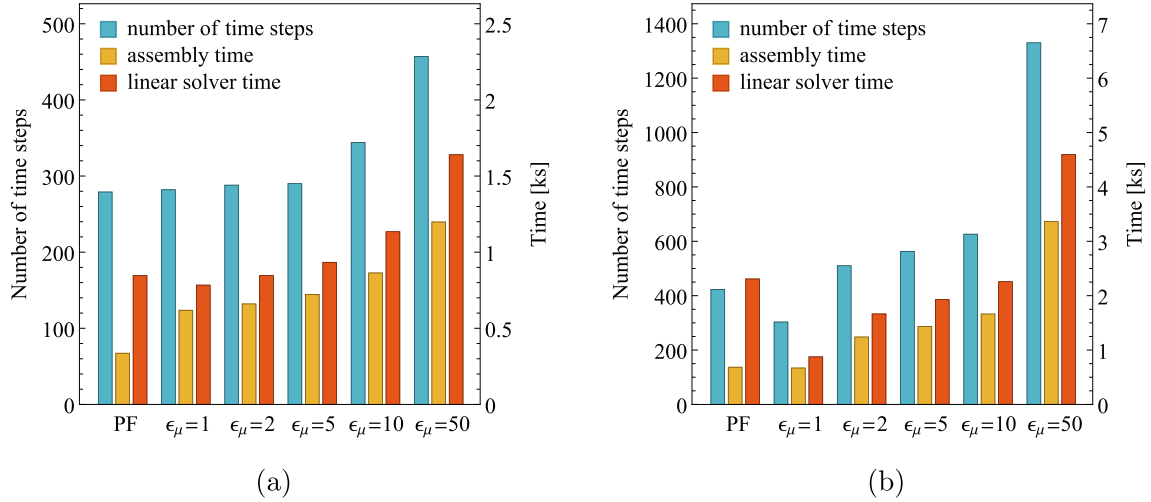

Fig. 4. Numerical study #1: comparison of the computational performance of the μPF model with the PF model for different values of the micromorphic penalty parameter ϵ_μ (given in GPa) in the case of (a) the viscous dissipation and (b) the mixed-type dissipation.

ϵ_μ (say for $\epsilon_\mu \leq 5$ GPa) exhibits a level of robustness close to that of the PF model. Recall that an adaptive time-stepping strategy is employed in the computations, thus the total number of time steps can be used as an indicator of the robustness of the computational scheme. Concerning the linear-solver time, the performance of the μPF model with moderate ϵ_μ is similar to that of the PF model. Regarding the assembly time, i.e. the time needed to assemble the global residual vector and the global tangent matrix, the PF model outperforms the μPF model for all ϵ_μ. This is expected since, unlike in the PF model, at each iteration in the μPF model, the local problem (49) is solved at each Gauss point.

On the other hand, in the case of the mixed-type dissipation, the μPF model outperforms the PF model in terms of the linear-solver time for a wide range of ϵ_μ between 1 and 10 GPa, and only for very large $\epsilon_\mu = 50$ GPa the linear-solver time is visibly higher for the μPF model. The reason is that the total number of unknowns for the PF model, which additionally involves the Lagrange multipliers as the global unknowns, is higher, and hence the increased linear-solver time. It can be seen that for relatively small values of ϵ_μ, namely $\epsilon_\mu = 1$ and 2 GPa, the total CPU time (the sum of the assembly and linear-solver times) is lower for the μPF model than for the PF model.

In the analysis above, a simple case with only one order parameter has been considered in order to illustrate the main features of the μPF model. We have also examined the computational performance of the PF and μPF models for more complex cases of two and four order parameters. The results, not reported here in detail, show that, in the case of the viscous dissipation, PF and μPF models perform nearly the same, and the general features reported above apply also in the case of multiple order parameters. However, in

the case of the mixed-type dissipation, the computational performance of the PF model was considerably weaker compared to the corresponding μPF model. Firstly, since the Lagrange multipliers are the global unknowns in the conventional formulation, the computational cost of the linear solver increases significantly. More importantly, severe convergence issues are encountered when the rate-independent dissipation is included in the PF model. In fact, the corresponding simulations could not be completed due to the failure of the Newton scheme.

In conclusion, the results reported above and our supplementary computations demonstrate the superior performance of the micromorphic formulation over the conventional one in the case of a more complex evolution law, such as the one associated with the mixed-type dissipation. The superiority is significantly more pronounced in the case of multiple order parameters.

5.3. Numerical study #2: the effect of the rate-independent dissipation

The second study focuses on the physical aspects of the rate-independent dissipation. For this purpose, we examine the effect of the rate-independent threshold κ_i, see Eq. (54), on the microstructure evolution during nano-indentation and on the associated indentation load–depth response for a system with 5 phases, i.e. for the square-to-parallelogram transformation with 4 variants of martensite. As the baseline for the study, we consider the case of the viscous dissipation, which has been previously studied by using the conventional phase-field model (Rezaee-Hajidehi and Stupkiewicz, 2020). For consistency, the corresponding simulation has been also performed here by using the presented micromorphic phase-field model. A related study, limited to only one

order parameter, has been performed by Tůma et al. (2018), where the effect of the rate-independent dissipation has been examined for a pseudoelastic micro-pillar subjected to compression.

The computational domain is set to $W \times H = 1000 \times 1000$ nm^2 and the element size to $h = 1.8$ nm. In contrast to the previous example, we do not impose the symmetry constraint so that the simulations are performed for the entire computational domain. Accordingly, the total number of elements is about 300 000 resulting in the total number of degrees of freedom of approximately 1.8 million. The radius of the indenter is adopted as $R = 50$ nm and the maximum indentation depth is prescribed to $\delta_{max} = 30$ nm.

Note that a spontaneous microstructure symmetry breakdown, which may occur as an energy-lowering mechanism, has been encountered for the system under study (Rezaee-Hajidehi and Stupkiewicz, 2020). Hence, the symmetry of the setup is not exploited here. As it is discussed later, in a few cases investigated here, the microstructure indeed develops in a non-symmetric manner.

The martensite variants associated with the square-to-parallelogram transformation are characterized by the non-symmetric transformation deformation tensors,

$$\mathbf{F}_1^t = \begin{pmatrix} \alpha & -\gamma \\ 0 & \beta \end{pmatrix}, \quad \mathbf{F}_2^t = \begin{pmatrix} \alpha & \gamma \\ 0 & \beta \end{pmatrix}, \quad \mathbf{F}_3^t = \begin{pmatrix} \beta & 0 \\ -\gamma & \beta \end{pmatrix}, \quad \mathbf{F}_4^t = \begin{pmatrix} \beta & 0 \\ \gamma & \beta \end{pmatrix},$$
(74)

where the stretch parameters $\alpha = 1.05$ and $\beta = 0.95$ are assumed as in the previous example and the shear parameter $\gamma = 0.05$ is adopted. Thereby, in analogy to Eq. (33), the transformation deformation gradient is defined as $\mathbf{F}^t = \eta_0 \mathbf{I} + \sum_{i=1}^{N} \eta_i \mathbf{F}_i^t$.

Simulations are carried out for different values of the rate-independent threshold, namely $\kappa_i = \kappa = 2, 5$ and 10 MPa. Following the computational study reported in Section 5.2, the micromorphic penalty parameter $\epsilon_\mu = 5$ GPa is adopted, see Figs. 3 and 4. The other material and model parameters are the same as those specified in Section 5.1.

Selected snapshots of the microstructure evolution along with the P–δ responses are depicted in Fig. 5. The microstructure is represented by the martensite variant domains of the volume fraction $\eta_i \geqslant 0.5$. Each martensite variant i, denoted by Vi, is recognized by a specific color, while the remaining white space is occupied by the austenite. It has been observed that in all cases the microstructure

evolves in a qualitatively similar fashion. The transformation initiates by a concurrent nucleation of all martensite variants, followed by their subsequent growth in a symmetric manner. During unloading, all the martensite variants shrink simultaneously, again in a symmetric manner.

The effect of the rate-independent dissipation is qualitatively similar to that briefly described in Section 5.2 for the case with two phases, but here in a more pronounced way, with the maximum effect observed for $\kappa = 10$ MPa (the microstructure evolution for $\kappa = 2$ and 5 MPa exhibits a similar, but weaker effect, and thus is not shown in Fig. 5(a)). The first observation is that the area of the hysteresis loop becomes larger as κ increases, see Fig. 5(b). At the same time, the forward transformation initiates and proceeds at a higher indentation load P. Accordingly, the size of the transformed domain during loading is smaller compared to that of the viscous dissipation at the same indentation depth δ. The situation is more complex during unloading. At the beginning of unloading, due to the viscous contribution in the dissipation potential, the transformed domain continues to grow in size, with the largest growth observed for the viscous dissipation. An elastic response is then observed for the mixed-type dissipation (although this is not clearly visible in the P–δ response). The extent of the elastic response increases as κ increases, and the reverse transformation initiates when the driving force overcomes the rate-independent threshold. This is in contrast to the viscous dissipation, where the reverse transformation occurs with no intermediate purely elastic response. To better delineate these observations, the evolution of the area of the transformed domain is shown in Fig. 6. Interestingly, for a very high rate-independent threshold $\kappa = 20$ MPa, an almost complete arrest of the reverse transformation is observed during unloading.

It has been observed that for $\kappa = 10$ MPa, the indenter separates from the contact surface during unloading at the indentation depth of about $\delta = 8$ nm. Approximately at this instant, two small nuclei of variants V1 and V2 appear, see the arrows pointing upward in Fig. 5(a) indicating the nucleation sites, and immediately vanish as the transformed domain shrinks further.

The effect of the indentation speed v has been also studied and the results are presented in Fig. 7. Lower indentation speeds, $v = 1.5$ and 0.5 nm/s, have been examined, and the corresponding
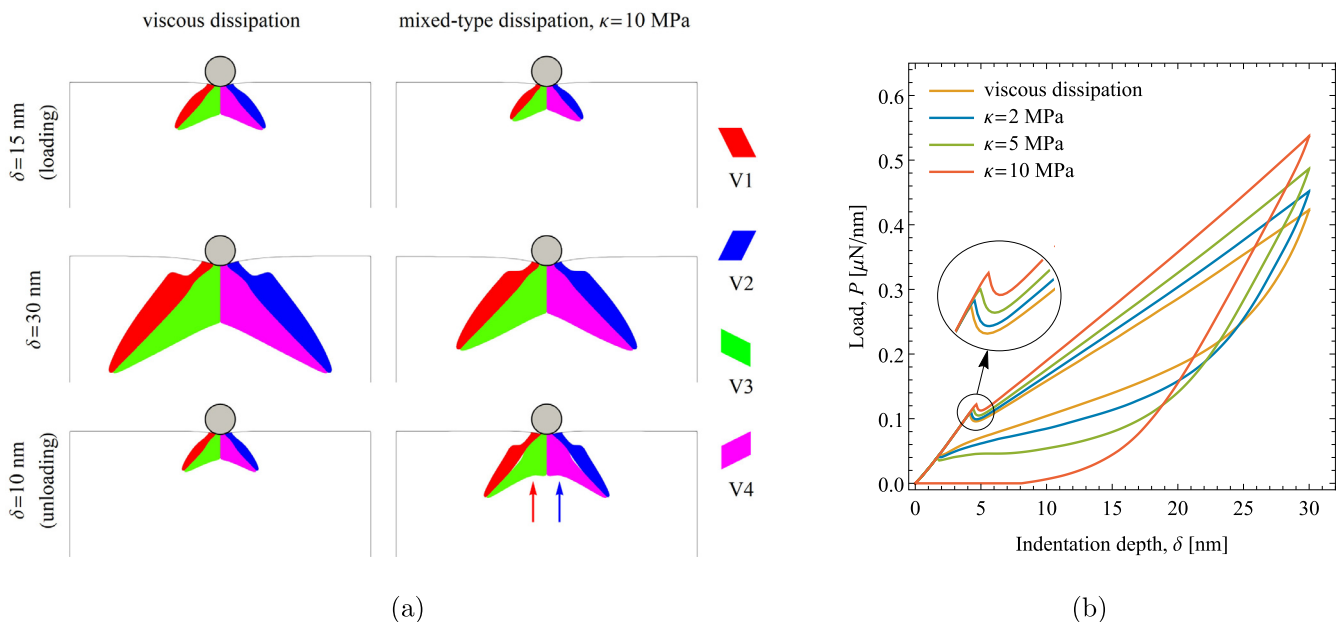

(a)   (b)

Fig. 5. Numerical study #2: the effect of the rate-independent dissipation on (a) the microstructure evolution and (b) the P–δ response.
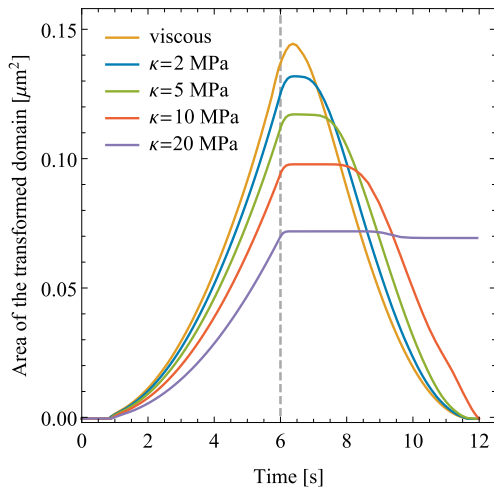
Fig. 6. Numerical study #2: time evolution of the area of the transformed domain. The dashed line indicates the end of the loading stage.

simulations have been carried out for the viscous dissipation and for the mixed-type dissipation with $\kappa = 5$ MPa. The results show that as v decreases, the area of the hysteresis loop decreases, such that for the viscous dissipation the area tends to zero (except for the initial nucleation event, which is only slightly dependent on v). However, for the mixed-type dissipation, the area of the hysteresis loop approaches a finite value, which is controlled by the rate-independent threshold κ. Similar effects have been reported by Tůma et al. (2018) and, in the case of the viscous dissipation, by Rezaee-Hajidehi and Stupkiewicz (2020).

It is worthwhile to mention that the microstructure symmetry breakdown has been observed in some cases, namely for the viscous dissipation with $v = 1.5$ and 0.5 nm/s and for the mixed-type dissipation with $v = 0.5$ nm/s. In fact, the sudden load rise, which appears in the corresponding P–δ responses during unloading, is associated with the annihilation of the martensite variant V2, see the inset in Fig. 7(b).

Finally, to illustrate the performance of the micromorphic formulation, the difference between the order parameters $\boldsymbol{\eta}$ and their micromorphic counterparts $\boldsymbol{\chi}$, measured by the norm $\|\boldsymbol{\eta} - \boldsymbol{\chi}\|$, is
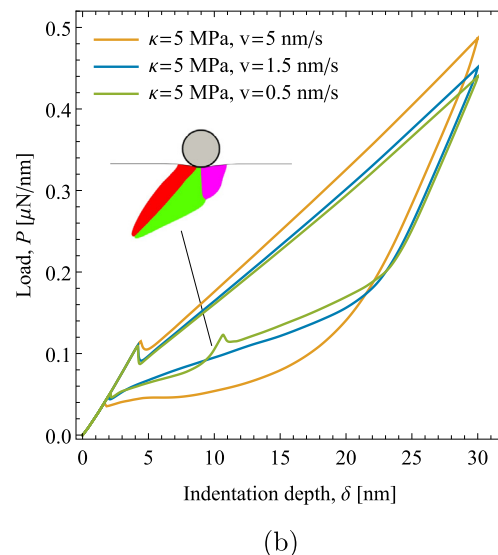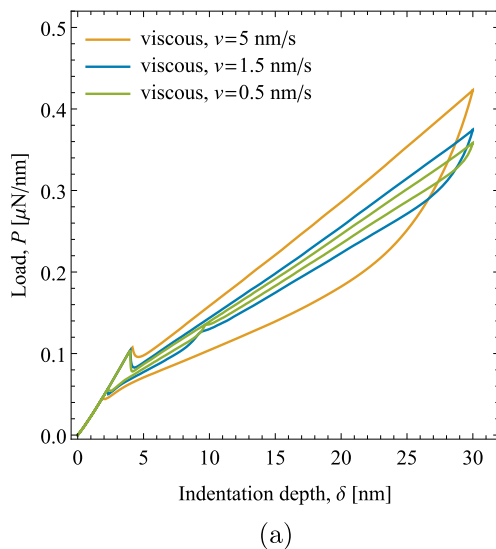
depicted in Fig. 8. It shows that the difference is small, with the maximum value of 0.023, which is consistent with that obtained for the case with a single order parameter, see the snapshot related to $\epsilon_\mu = 5$ GPa in Fig. 3. It can be observed that the difference is larger within the austenite–martensite interfaces compared to the martensite–martensite interfaces, which is possibly related to a higher interfacial energy of the austenite–martensite interfaces.

5.4. Numerical study #3: relaxation and rearrangement of self-accommodated martensite

In the previous study, we have shown how the microstructure evolution and the related pseudoelastic response are affected by the rate-independent dissipation. With the aim to provide further insights, in this study we extend the setup of the previous example and apply the indentation load to a relaxed self-accommodated martensite microstructure. In order to ensure that the martensite is a stable phase in the stress-free conditions and the austenite does not develop during the relaxation stage, the chemical energy of transformation is set to a negative value, $\Delta F^0 = -20$ MPa. The initial state of the system is then generated by a random distribution of the order parameters η_i within the entire computational domain. Specifically, each random assignment of the Gauss-point values corresponds either to $0.4 \leqslant \eta_1 \leqslant 0.6$ (with $\eta_2 = 1 - \eta_1$) or to $0.4 \leqslant \eta_3 \leqslant 0.6$ (with $\eta_4 = 1 - \eta_3$), while $\eta_0 = 0$ everywhere. Note that the same initial random seed has been used in all the computations. The microstructure is then allowed to evolve in time (with no external loading applied) until a relaxed (steady-state) microstructure is reached. Subsequently, the resulting relaxed self-accommodated microstructure is subjected to an indentation loading–unloading cycle.

The procedure described above is roughly equivalent to a very quick cooling of the system below the transformation temperature. Although the extension of the model to the thermomechanically coupled case is rather straightforward, such an extension is not attempted here and the (uniform) temperature is controlled implicitly by varying the chemical energy.

To allow formation of fine microstructures (especially at the early stage of the relaxation when the microstructure evolves from the initial random state), the interfaces are chosen to be thinner. Accordingly, the interface thickness parameter is reduced by one
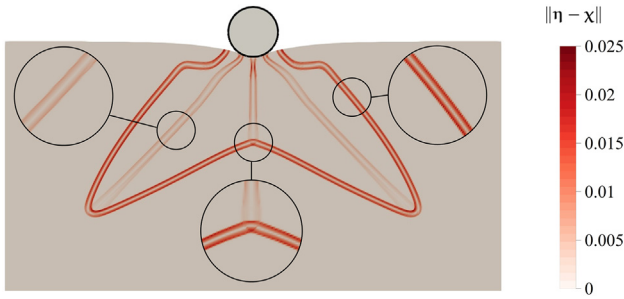

(a)

(b)

Fig. 7. Numerical study #2: the effect of the indentation speed v on the P–δ response for (a) the viscous dissipation and (b) the mixed-type dissipation with $\kappa = 5$ MPa. The inset in panel (b) shows the non-symmetric microstructure at the final stage of unloading for $v = 0.5$ nm/s.

Fig. 8. Numerical study #2: distribution of the difference between $\boldsymbol{\eta}$ and $\boldsymbol{\chi}$, measured by $\|\boldsymbol{\eta} - \boldsymbol{\chi}\|$, at the indentation depth $\delta = 30$ nm (mixed-type dissipation, $\kappa = 5$ MPa).

half, i.e. $\ell_{ij} = \ell = 2$ nm (and thus the theoretical interface thickness is equal to $\pi\ell \approx 6.3$ nm). To gain a sufficient resolution of the interfaces, the element size is set to $h = 1.5$ nm, which leads to the total number of elements of approximately 445 000 and the total number of degrees of freedom of approximately 2.7 million. A bigger indenter with the radius $R = 150$ nm is considered, so that, as it is shown below, the microstructure rearrangement during the indentation cycle extends over a larger portion of the microstructure.

During the relaxation process, the microstructure evolves until a steady state is achieved. Note that the local driving forces for transformation are not necessarily equal to zero in the steady state, but further microstructure evolution is stopped due to the threshold on the driving force that results from the rate-independent dissipation. The variation of the total elastic strain energy $\mathcal{F}_{\text{el}} = \int_B F_{\text{el}} dV$ and the total interfacial energy $\mathcal{F}_{\text{int}} = \int_B F_{\text{int}} dV$ during the relaxation stage are illustrated in Fig. 9(a) where the sum of the two contributions, $\mathcal{F}_{\text{el}} + \mathcal{F}_{\text{int}}$, as well as $\mathcal{F}_{\text{el}}$ alone are shown (note that the chemical energy F_{chem} is constant and is not included in the figure).

At the beginning, the interfacial energy is at its highest value, whereas the elastic strain energy is relatively small. As time progresses, the microstructure coarsens and hence the interfacial energy decreases significantly at the cost of a rapid increase of the elastic strain energy. Henceforth, while descending gradually,

both energy contributions tend towards a constant value. The effect of the rate-independent threshold κ is reflected on the level of coarsening of the microstructure during relaxation. It can be seen that, as κ decreases, the relaxed microstructure becomes coarser, see the corresponding snapshots in Fig. 10, and thus it takes a longer physical time for the system to achieve the steady state.

Note that the computational cost varies depending on the value of the rate-independent threshold κ. For the lowest $\kappa = 2$ MPa, which was the most computationally demanding case, the relaxation process took nearly 96 hours, as compared to about 39 hours for $\kappa = 10$ MPa.

Fig. 10 depicts the microstructure rearrangement during the indentation loading–unloading cycle. It can be seen that, as expected, the microstructure rearrangement mainly takes place in the area close to the indenter, while only some minor changes are noted at the bottom part of the domain. The overall pattern of the final microstructure (in terms of the distribution and shape of the martensite variants) is qualitatively similar in all cases, see the snapshots corresponding to $\delta = 30$ nm in Fig. 10, and does not really resemble that observed in the previous example, see Fig. 5. Although the microstructure changes slightly during unloading, the response is mostly elastic. In all cases, around the indentation depth of $\delta = 22$ nm during unloading, the indenter is separated from the contact surface (the corresponding snapshots are denoted as $P = 0$ in Fig. 10), and as time advances, no further appreciable change in the microstructure is observed.

A number of distinct events, e.g. in the form of a sudden load drop, are apparent in the indentation P–δ responses, see Fig. 9(b). These events typically reflect prominent changes of the microstructure during the rearrangement. It is also evident that the dependence of the P–δ response on κ does not follow a consistent trend. This is related to the fact that the relaxed microstructures are significantly different for each κ, and the subsequent microstructure rearrangement is accompanied by events with qualitatively different features.

To illustrate the effect of the rate-independent threshold κ on the P–δ response, we have performed an additional study in which the same relaxed microstructure (the coarsest one, obtained for $\kappa = 2$ MPa) is used for all simulations. The corresponding results are presented in Fig. 11. It follows that, except for some marginal
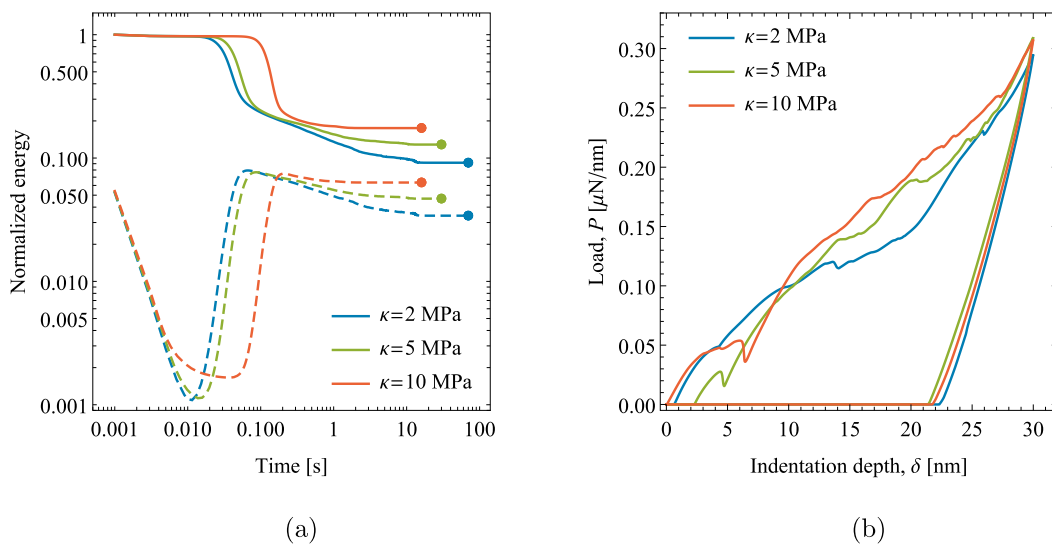

(a)

(b)

Fig. 9. Numerical study #3: (a) variation of the sum $\mathcal{F}_{\text{el}} + \mathcal{F}_{\text{int}}$ (solid lines) and $\mathcal{F}_{\text{el}}$ (dashed lines) over time during the relaxation stage and (b) the P–δ response during indentation. The energy contributions are normalized by the initial value of $\mathcal{F}_{\text{el}} + \mathcal{F}_{\text{int}}$. The circles in panel (a) indicate the instant at which the steady state is achieved, after which the indentation load is applied.
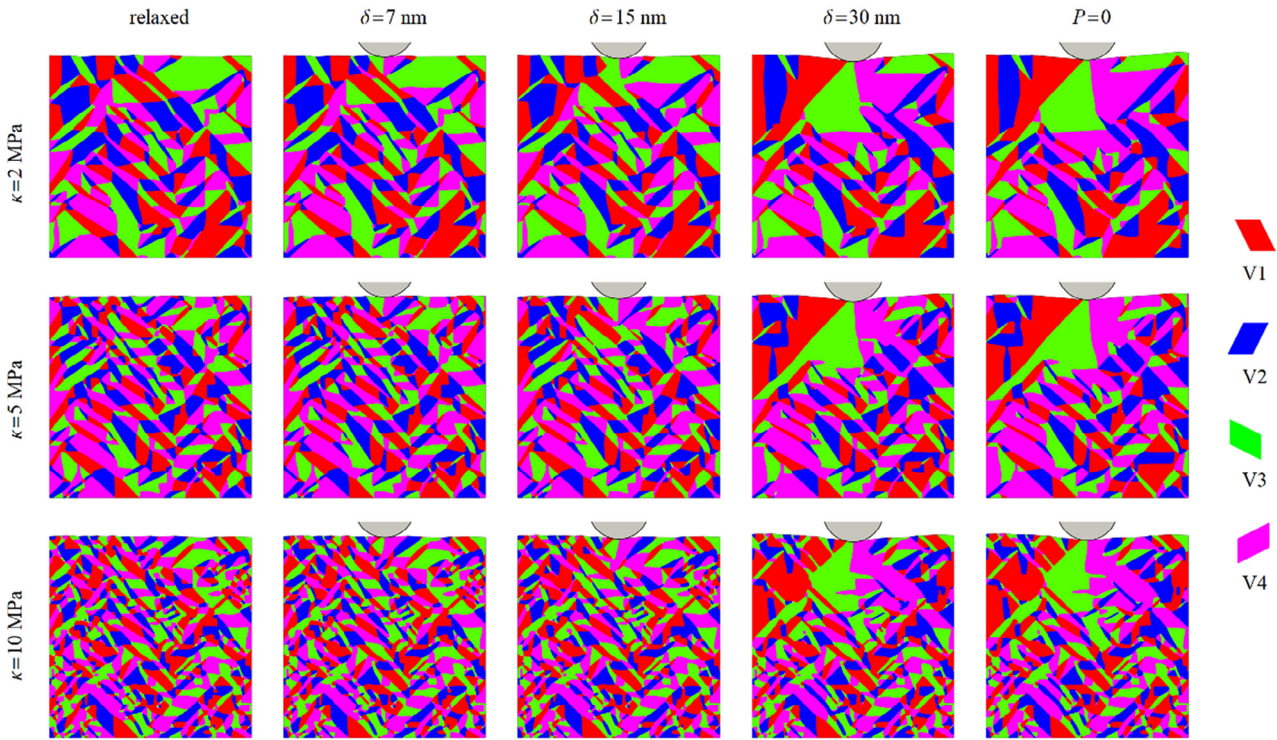
Fig. 10. Numerical study #3: the effect of the rate-independent threshold κ on the relaxed microstructure and the indentation-induced microstructure rearrangement.
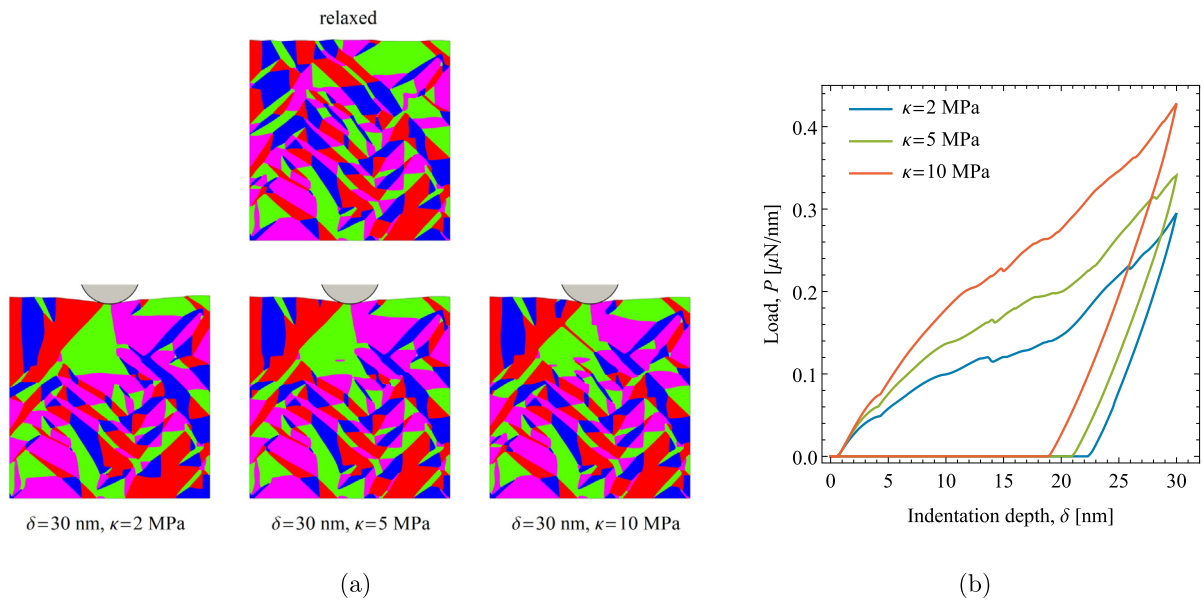

Fig. 11. Numerical study #3: the effect of κ on the microstructure rearrangement (a) and the P–δ response (b) when indentation is performed for the same initial relaxed microstructure. For the color coding of the martensite variants, see the legend in Fig. 10.

changes, the microstructure at the maximum indentation depth $\delta = 30$ nm is essentially the same for all κ. At the same time, the same sequence of events is observed in all P–δ responses. It can also be seen that, as κ increases, the microstructure rearrangement proceeds at a higher load P, similar to what has been observed in the previous study, see Fig. 5.

The full transformation cycle is accomplished by inducing the reverse transformation to the austenite via heating. Here, the temperature is implicitly controlled by increasing the chemical energy of transformation to $\Delta F^0 = 200$ MPa. Subsequently, the system is allowed to evolve in time. Note that a large value of ΔF^0, which is equivalent to severe overheating, is needed in order to overcome the transformation barrier of the double-obstacle potential and thus to initiate the reverse transformation. The full transformation cycle for the case with $\kappa = 5$ MPa is illustrated in Fig. 12. During the heating-up process, the nucleation of the austenite occurs at several places, and eventually the stress-free austenite state is recovered. Note that the reverse transformation is completed in a relatively short time, as a result of the severe overheating and the related high driving force for transformation.
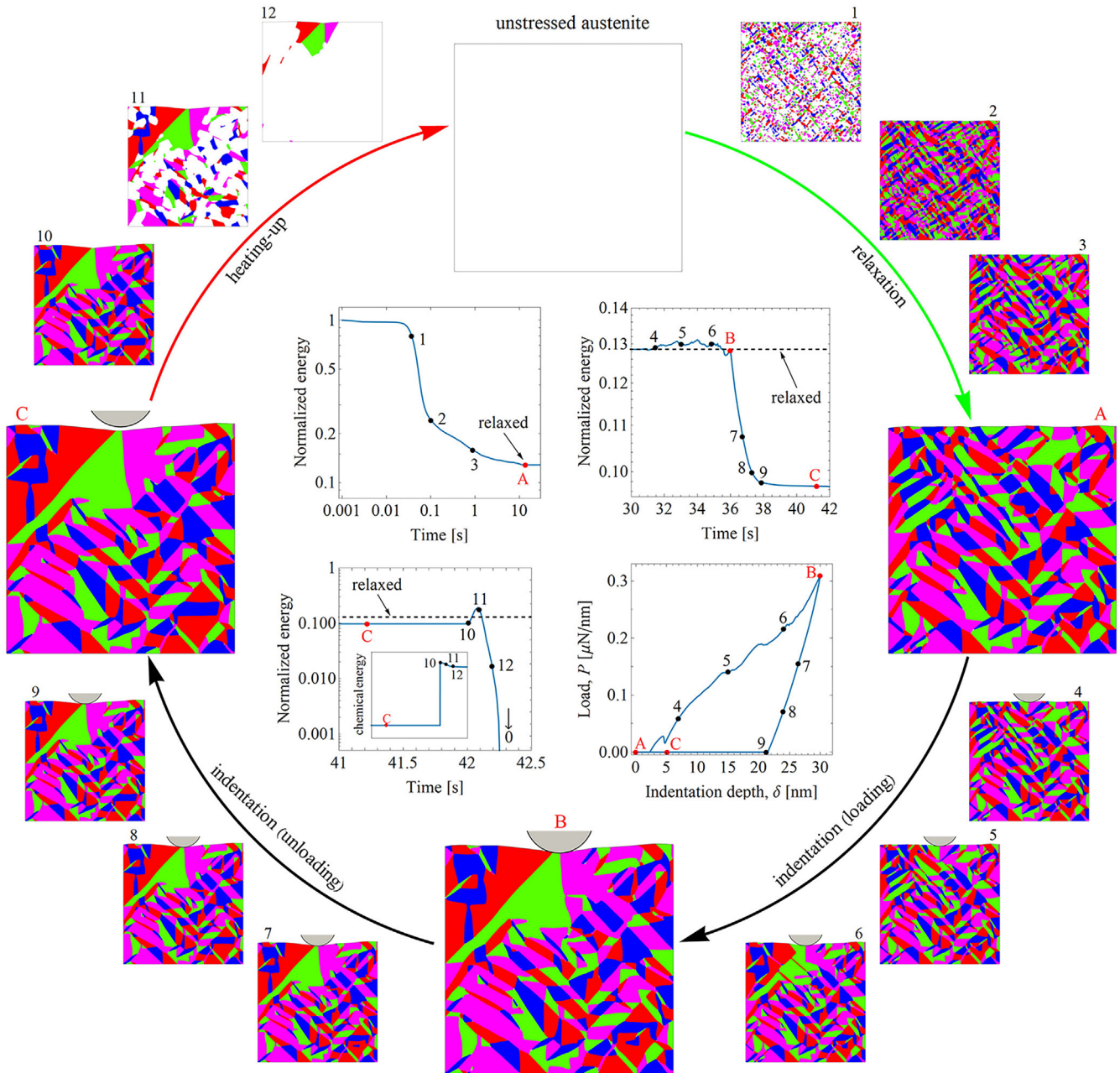
Fig. 12. Numerical study #3: the full transformation cycle for $\kappa = 5$ MPa. The white areas in snapshot 1 represent the diffuse interfaces between the martensite variants, while those in snapshops 11 and 12 represent the austenite. For the color coding of the martensite variants, see the legend in Fig. 10.

6. Conclusion

We have employed the micromorphic approach to reformulate the phase-field model of multivariant martensitic transformation such that the microstructure evolution equations can be solved locally at each material point. This is in contrast to the conventional formulation in which microstructure evolution is governed by partial differential equations that must be solved on the global level. The micromorphic formulation is computationally beneficial, for instance, when the evolution equations are more complex than those corresponding to the simple and commonly used viscous dissipation. The complexity is thereby shifted to the local level where it can be handled in a more efficient and robust manner.

As an illustration, we have applied the micromorphic approach to the finite-strain multivariant phase-field model with the mixed-type dissipation in which the dissipation potential combines viscous and rate-independent contributions. The minimization problem which results from the incremental energy minimization framework is then non-smooth due to the rate-independent dissipation term. We have used the augmented Lagrangian method to transform the non-smooth minimization problem to a smooth and unconstrained saddle-point problem that in the finite-element setting can be efficiently solved locally at the Gauss-point level. The corresponding conventional formulation, which leads to a global saddle-point problem, can also be developed; however, it is not competitive to the micromorphic one in terms

of robustness and computational efficiency, especially when multiple order parameters are considered.

Declaration of Competing Interest

The authors declare that they have no known competing financial interests or personal relationships that could have appeared to influence the work reported in this paper.

Acknowledgement

Appendix A. Augmented Lagrangian treatment of rate-independent dissipation

A.1. Primal and dual formulation

In order to make the presentation concise, the formulation is provided here in the rate form. The incremental finite-step form can then be obtained by introducing the approximation $\dot{\boldsymbol{\eta}} \approx \Delta\boldsymbol{\eta}/\Delta t$. In the notation, we disregard the hat indicating the condensed variables, i.e. $\hat{\boldsymbol{\eta}} \to \boldsymbol{\eta}$ and likewise for other variables and the related functions. In addition, for simplicity, only the rate-independent dissipation is taken into account, i.e. $D^{\mathrm{v}} = 0$.

In the rate formulation, the local (pointwise) minimization problem, cf. Eq. (60), takes the form

$$\pi^{\mathrm{pen}}(\dot{\boldsymbol{\eta}}) = \frac{\mathrm{d}}{\mathrm{d}t}\left(F(\mathbf{F},\boldsymbol{\eta},\boldsymbol{\chi},\nabla\boldsymbol{\chi}) + I^{\mathrm{pen}}_{\Delta}(\boldsymbol{\eta})\right) + D^{\mathrm{in}}(\dot{\boldsymbol{\eta}}) \quad \to \quad \min, \quad (A.1)$$

where $D^{\mathrm{in}}(\dot{\boldsymbol{\eta}}) = \|\dot{\boldsymbol{\eta}}\|_{\mathbf{D}} = \sqrt{\dot{\boldsymbol{\eta}}\cdot\mathbf{D}\dot{\boldsymbol{\eta}}}$ and $\mathbf{D}$ is a symmetric positive-definite matrix. Neglecting the terms that do not depend on $\dot{\boldsymbol{\eta}}$, the rate-potential π^{pen} can be rewritten in the form

$$\pi^{\mathrm{pen}}(\dot{\boldsymbol{\eta}}) = -\mathbf{f}\cdot\dot{\boldsymbol{\eta}} + D^{\mathrm{in}}(\dot{\boldsymbol{\eta}}), \qquad \mathbf{f} = -\frac{\partial\left(F + I^{\mathrm{pen}}_{\Delta}\right)}{\partial\boldsymbol{\eta}}, \quad (A.2)$$

where $\mathbf{f}$ is the thermodynamic driving force conjugate to $\boldsymbol{\eta}$.

Minimization of π^{pen} leads to the following inclusion, which can also be written in the dual form,

$$\mathbf{f} \in \partial D^{\mathrm{in}}(\dot{\boldsymbol{\eta}}), \qquad \dot{\boldsymbol{\eta}} \in \partial I_{\mathcal{C}}(\mathbf{f}), \quad (A.3)$$

where $I_{\mathcal{C}}$ is the indicator function of the convex set $\mathcal{C}$ such that $I^*_{\mathcal{C}} = D^{\mathrm{in}}$ is the Fenchel conjugate of the indicator function $I_{\mathcal{C}}$, and ∂D^{in} and $\partial I_{\mathcal{C}}$ are the subdifferentials of D^{in} and $I_{\mathcal{C}}$, respectively, see Moreau (1970), Rockafellar (1970). It can be checked that the convex set $\mathcal{C}$ is given by

$$\mathcal{C} = \left\{\mathbf{f}\in\mathcal{R}^N: \ \|\mathbf{f}\|_{\mathbf{D}^{-1}} \leqslant 1\right\}, \quad (A.4)$$

where $\|\mathbf{f}\|_{\mathbf{D}^{-1}} = \sqrt{\mathbf{f}\cdot\mathbf{D}^{-1}\mathbf{f}}$.

As an illustration, consider the case of active transformation with non-zero $\dot{\boldsymbol{\eta}}$, i.e. $\|\dot{\boldsymbol{\eta}}\| > 0$. The inclusions in Eq. (A.3) imply then

$$\mathbf{f} = \frac{\mathbf{D}\dot{\boldsymbol{\eta}}}{\|\dot{\boldsymbol{\eta}}\|_{\mathbf{D}}}, \qquad \dot{\boldsymbol{\eta}} = \zeta\mathbf{D}^{-1}\mathbf{f}, \quad (A.5)$$

where the multiplier $\zeta > 0$ is immediately found to be equal to $\zeta = \|\dot{\boldsymbol{\eta}}\|_{\mathbf{D}}$. For $\|\dot{\boldsymbol{\eta}}\| = 0$, we have $\mathbf{f}\in\mathcal{C}$.

A.2. Transformed variables and augmented Lagrangian formulation

We now introduce the transformed variables $\dot{\boldsymbol{\eta}}'$ and $\mathbf{f}'$,

$$\dot{\boldsymbol{\eta}}' = \mathbf{D}^{1/2}\dot{\boldsymbol{\eta}}, \qquad \mathbf{f}' = \mathbf{D}^{-1/2}\mathbf{f}, \quad (A.6)$$

such that $\|\dot{\boldsymbol{\eta}}\|_{\mathbf{D}} = \|\dot{\boldsymbol{\eta}}'\|$ and $\|\mathbf{f}\|_{\mathbf{D}^{-1}} = \|\mathbf{f}'\|$. Note that, with this transformation, the convex set $\mathcal{C}$ becomes a unit ball in $\mathcal{R}^N$,

$$\mathcal{C}' = \left\{\mathbf{f}'\in\mathcal{R}^N: \ \|\mathbf{f}'\| \leqslant 1\right\}, \quad (A.7)$$

and Eq. (A.5)$_1$ takes the form

$$\mathbf{f}' = \frac{\dot{\boldsymbol{\eta}}'}{\|\dot{\boldsymbol{\eta}}'\|} \qquad \text{when } \|\dot{\boldsymbol{\eta}}'\| > 0. \quad (A.8)$$

Accordingly, the minimization problem (A.1) converts to

$$\pi'(\dot{\boldsymbol{\eta}}') = -\mathbf{f}'\cdot\dot{\boldsymbol{\eta}}' + \|\dot{\boldsymbol{\eta}}'\| \quad \to \quad \min. \quad (A.9)$$

To efficiently solve the above minimization problem, we employ the augmented Lagrangian technique and develop a formulation based on that of Alart and Curnier (1991) for the case of pure friction, see also Pietrzak and Curnier (1999). The minimization problem (A.9) is thus replaced by a smooth and unconstrained saddle-point problem

$$\{\dot{\boldsymbol{\eta}}',\boldsymbol{\lambda}'\} = \arg\min_{\dot{\boldsymbol{\eta}}'}\max_{\boldsymbol{\lambda}'}\ \mathcal{L}'(\dot{\boldsymbol{\eta}}',\boldsymbol{\lambda}'), \quad (A.10)$$

formulated for the following Lagrangian,

$$\mathcal{L}'(\dot{\boldsymbol{\eta}}',\boldsymbol{\lambda}') = -\mathbf{f}'\cdot\dot{\boldsymbol{\eta}}' + L'(\dot{\boldsymbol{\eta}}',\boldsymbol{\lambda}'), \quad (A.11)$$

where

$$L'(\dot{\boldsymbol{\eta}}',\boldsymbol{\lambda}') = \begin{cases} \left(\boldsymbol{\lambda}' + \frac{1}{2}\varrho\dot{\boldsymbol{\eta}}'\right)\cdot\dot{\boldsymbol{\eta}}' & \text{if } \|\boldsymbol{\lambda}'_{\mathrm{aug}}\| \leqslant 1, \\ -\frac{1}{2\varrho}\left(\|\boldsymbol{\lambda}'\|^2 - 2\|\boldsymbol{\lambda}'_{\mathrm{aug}}\| + 1\right) & \text{otherwise}. \end{cases} \quad (A.12)$$

Here, $\boldsymbol{\lambda}'$ is the vector of Lagrange multipliers, $\boldsymbol{\lambda}'_{\mathrm{aug}} = \boldsymbol{\lambda}' + \varrho\dot{\boldsymbol{\eta}}'$ is the augmented Lagrange multiplier, and $\varrho > 0$ is a regularization parameter. Since L' is a continuously differentiable function, the solution of the saddle-point problem (A.10) can be found by solving the equations expressing the stationarity of $\mathcal{L}'$, viz.

$$\frac{\partial\mathcal{L}'}{\partial\dot{\boldsymbol{\eta}}'} = -\mathbf{f}' + \frac{\partial L'}{\partial\dot{\boldsymbol{\eta}}'} = \mathbf{0}, \qquad \frac{\partial\mathcal{L}'}{\partial\boldsymbol{\lambda}'} = \frac{\partial L'}{\partial\boldsymbol{\lambda}'} = \mathbf{0}. \quad (A.13)$$

It can be checked that, at the solution of Eqs. (A.13), the Lagrange multiplier $\boldsymbol{\lambda}'$ is equal to the driving force $\mathbf{f}'$, i.e. $\mathbf{f}' = \boldsymbol{\lambda}'$, and $\mathbf{f}'$ satisfies the inclusion $\mathbf{f}' \in \partial I^*_{\mathcal{C}'}$ that results from the minimization problem (A.9). Importantly, the solution does not depend on the regularization parameter ϱ, and the method does not introduce any approximation.

The augmented Lagrangian formulation of the original minimization problem (A.1) is obtained by transforming the variables back to the physical space, i.e. $\dot{\boldsymbol{\eta}} = \mathbf{D}^{-1/2}\dot{\boldsymbol{\eta}}'$, $\mathbf{f} = \mathbf{D}^{1/2}\mathbf{f}'$ and $\boldsymbol{\lambda} = \mathbf{D}^{1/2}\boldsymbol{\lambda}'$. In particular, function L' in Eq. (A.12) can in this way be transformed to function L^{in} in Eq. (62).

References

Ahluwalia, R., Lookman, T., Saxena, A., Albers, R.C., 2004. Landau theory for shape memory polycrystals. Acta Mater. 52, 209–218.

Alart, P., Curnier, A., 1991. A mixed formulation for frictional contact problems prone to newton like solution methods. Comp. Meth. Appl. Mech. Eng. 92, 353–375.

Anand, L., Aslan, O., Chester, S.A., 2012. A large-deformation gradient theory for elastic–plastic materials: strain softening and regularization of shear bands. Int. J. Plast. 30, 116–143.

Artemev, A., Wang, Y., Khachaturyan, A.G., 2000. Three-dimensional phase field model and simulation of martensitic transformation in multilayer systems under applied stresses. Acta Mater. 48, 2503–2518.

Aslan, O., Cordero, N., Gaubert, A., Forest, S., 2011. Micromorphic approach to single crystal plasticity and damage. Int. J. Eng. Sci. 49, 1311–1325.

Bartels, A., Mosler, J., 2017. Efficient variational constitutive updates for Allen–Cahn-type phase field theory coupled to continuum mechanics. Comp. Meth. Appl. Mech. Eng. 317, 55–83.

Bhattacharya, K., 2003. Microstructure of Martensite: Why It Forms and How It Gives Rise to the Shape-memory Effect. Oxford University Press, Oxford.

Borukhovich, E., Engels, P.S., Böhlke, T., Shchyglo, O., Steinbach, I., 2014. Large strain elasto-plasticity for diffuse interface models. Model. Simul. Mater. Sci. Eng. 22, 034008.

Carstensen, C., Hackl, K., Mielke, A., 2002. Non–convex potentials and microstructures in finite–strain plasticity. Proc. Roy. Soc. Lond. A 458, 299–317.

Clayton, J.D., Knap, J., 2011. A phase field model of deformation twinning: Nonlinear theory and numerical simulations. Physica D 240, 841–858.

Di Leo, C.V., Rejovitzky, E., Anand, L., 2014. A Cahn–Hilliard-type phase-field theory for species diffusion coupled with large elastic deformations: application to phase-separating Li-ion electrode materials. J. Mech. Phys. Solids 70, 1–29.

Dimitrijevic, B.J., Hackl, K., 2008. A method for gradient enhancement of continuum damage models. Tech. Mech. 28, 43–52.

Engelen, R.A.B., Geers, M.G.D., Baaijens, F.P.T., 2003. Nonlocal implicit gradient-enhanced standard elasto-plasticity for the modelling of softening behaviour. Int. J. Plast. 19, 403–433.

Forest, S., 2009. Micromorphic approach for gradient elasticity, viscoplasticity, and damage. J. Eng. Mech. 135, 117–131.

Forest, S., 2016. Nonlinear regularization operators as derived from the micromorphic approach to gradient elasticity, viscoplasticity and damage. Proc. Roy. Soc. A 472, 20150755.

Hildebrand, F.E., Miehe, C., 2012. A phase field model for the formation and evolution of martensitic laminate microstructure at finite strains. Philos. Mag. 92, 4250–4290.

Hudobivnik, B., Korelc, J., 2016. Closed-form representation of matrix functions in the formulation of nonlinear material models. Finite Elem. Anal. Des. 111, 19–32.

Korelc, J., 2009. Automation of primal and sensitivity analysis of transient coupled problems. Comput. Mech. 44, 631–649.

Korelc, J., Wriggers, P., 2016. Automation of Finite Element Methods. Springer International Publishing, Switzerland.

Kružík, M., Mielke, A., Roubíček, T., 2005. Modelling of microstructure and its evolution in shape-memory-alloy single-crystals, in particular in CuAlNi. Meccanica 40, 389–418.

Levitas, V.I., Levin, V.A., Zingerman, K.M., Freiman, E.I., 2009. Displacive phase transitions at large strains: phase-field theory and simulations. Phys. Rev. Lett 103, 025702.

Levitas, V.I., Preston, D.L., 2002. Three-dimensional Landau theory for multivariant stress-induced martensitic phase transformations. I. Austenite↔martensite. Phys. Rev. B 66, 134206.

Mazière, M., Forest, S., 2015. Strain gradient plasticity modeling and finite element simulation of Lüders band formation and propagation. Continuum Mech. Thermodyn. 27, 83–104.

Michaleris, P., Tortorelli, D.A., Vidal, C.A., 1994. Tangent operators and design sensitivity formulations for transient non-linear coupled problems with applications to elastoplasticity. Int. J. Numer. Meth. Eng. 37, 2471–2499.

Miehe, C., 2011. A multi-field incremental variational framework for gradient-extended standard dissipative solids. J. Mech. Phys. Solids 59, 898–923.

Miehe, C., Aldakheel, F., Teichtmeister, S., 2017. Phase-field modeling of ductile fracture at finite strains: a robust variational-based numerical implementation of a gradient-extended theory by micromorphic regularization. Int. J. Numer. Meth. Eng. 111, 816–863.

Miehe, C., Lambrecht, M., Gürses, E., 2004. Analysis of material instabilities in inelastic solids by incremental energy minimization and relaxation methods: evolving deformation microstructures in finite plasticity. J. Mech. Phys. Solids 52, 2725–2769.

Miehe, C., Teichtmeister, S., Aldakheel, F., 2016. Phase-field modelling of ductile fracture: a variational gradient-extended plasticity-damage theory and its micromorphic regularization. Proc. Roy. Soc. A 374, 20150170.

Mielke, A., Roubíček, T., 2015. Rate-independent Systems. Springer, New York.

Moreau, J.J., 1970. Sur les lois de frottement, de plasticité et de viscosité. C.R. Acad. Sci. Paris A 271, 608–611.

Ortiz, M., Repetto, E.A., 1999. Nonconvex energy minimization and dislocation structures in ductile single crystals. J. Mech. Phys. Solids 47, 397–462.

Peerlings, R.H.J., de Borst, R., Brekelmans, W.A.M., de Vree, J.H.P., 1996. Gradient enhanced damage for quasi-brittle materials. Int. J. Numer. Meth. Eng. 39, 3391–3403.

Penrose, O., Fife, P.C., 1990. Thermodynamically consistent models of phase-field type for the kinetic of phase transitions. Physica D 43, 44–62.

Petryk, H., 1982. A consistent energy approach to defining stability of plastic deformation processes. In: Schroeder, F.H. (Ed.), IUTAM Symposium on Stability in the Mechanics of Continua. Springer, Berlin, Nümbrecht, pp. 262–272.

Petryk, H., 1985. On energy criteria of plastic instability. Plastic Instability, Proc. Considére Memorial. Ecole Nat. Ponts Chauss. Paris, 215–226.

Petryk, H., 1991. The energy criteria of instability in time-independent inelastic solids. Arch. Mech. 43, 519–545.

Petryk, H., 1993. Stability and constitutive inequalities in plasticity. In: Muschik, W. (Ed.), Non-Equilibrium Thermodynamics with Application to Solids, CISM Courses and Lectures, vol. 336. Springer, Wien, New York, pp. 259–329.

Petryk, H., 2003. Incremental energy minimization in dissipative solids. C. R. Mecanique 331, 469–474.

Petryk, H., 2020. A quasi-extremal energy principle for non-potential problems in rate-independent plasticity. J. Mech. Phys. Solids 136, 103691.

Petryk, H., Stupkiewicz, S., 2010. Interfacial energy and dissipation in martensitic phase transformations. Part I: theory. J. Mech. Phys. Solids 58, 390–408.

Petryk, H., Stupkiewicz, S., 2012. Instability of equilibrium of evolving laminates in pseudo-elastic solids. Int. J. Non-Linear Mech. 47, 317–330.

Pietrzak, G., Curnier, A., 1999. Large deformation frictional contact mechanics: continuum formulation and augmented lagrangian treatment. Comput. Meth. Appl. Mech. Eng. 177, 351–381.

Poh, L.H., Sun, G., 2017. Localizing gradient damage model with decreasing interactions. Int. J. Numer. Meth. Eng. 110, 503–522.

Rezaee-Hajidehi, M., Stupkiewicz, S., 2018. Gradient-enhanced model and its micromorphic regularization for simulation of Lüders-like bands in shape memory alloys. Int. J. Solids Struct. 135, 208–218.

Rezaee-Hajidehi, M., Stupkiewicz, S., 2020. Phase-field modeling of multivariant martensitic microstructures and size effects in nano-indentation. Mech. Mater. 141, 103267.

Rezaee-Hajidehi, M., Tůma, K., Stupkiewicz, S., 2020. Gradient-enhanced thermomechanical 3D model for simulation of transformation patterns in pseudoelastic shape memory alloys. Int. J. Plast. 128, 102589.

Rockafellar, R.T., 1970. Convex Analysis. Princeton University Press, Princeton, New Jersey.

Ryś, M., Forest, S., Petryk, H., 2020. A micromorphic crystal plasticity model with the gradient-enhanced incremental hardening law. Int. J. Plast. 128, 102655.

Scherer, J.-M., Phalke, V., Besson, J., Forest, S., Hure, J., Tanguy, B., 2020. Lagrange multiplier based vs micromorphic gradient-enhanced rate-(in)dependent crystal plasticity modelling and simulation. Comput. Meth. Appl. Mech. Eng. 372, 113426.

Schmitt, R., Müller, R., Kuhn, C., Urbassek, H.M., 2013. A phase field approach for multivariant martensitic transformations of stable and metastable phases. Arch. Appl. Mech. 83, 849–859.

She, H., Liu, Y., Wang, B., Ma, D., 2013. Finite element simulation of phase field model for nanoscale martensitic transformation. Comput. Mech. 52, 949–958.

Shu, Y.C., Yen, J.H., 2008. Multivariant model of martensitic microstructure in thin films. Acta Mater. 56, 3969–3981.

Steinbach, I., 2009. Phase-field models in materials science. Model. Simul. Mater. Sci. Eng. 17, 073001.

Stupkiewicz, S., Petryk, H., 2013. A robust model of pseudoelasticity in shape memory alloys. Int. J. Numer. Meth. Eng. 93, 747–769.

Stupkiewicz, S., Petryk, H., 2016. A minimal gradient-enhancement of the classical continuum theory of crystal plasticity. Part II: size effects. Arch. Mech. 68, 487–513.

Suezawa, M., Sumino, K., 1976. Behaviour of elastic constants in Cu-Al-Ni alloy in the close vicinity of M_s-point. Scr. Metall. 10, 789–792.

Tůma, K., Rezaee-Hajidehi, M., Hron, J., Farrell, P.E., Stupkiewicz, S., 2021. Phase-field modeling of multivariant martensitic transformation at finite-strain: computational aspects and large-scale finite-element simulations. Comput. Meth. Appl. Mech. Eng. 377, 113705.

Tůma, K., Stupkiewicz, S., Petryk, H., 2016. Size effects in martensitic microstructures: finite-strain phase field model versus sharp-interface approach. J. Mech. Phys. Solids 95, 284–307.

Tůma, K., Stupkiewicz, S., Petryk, H., 2018. Rate-independent dissipation in phase-field modelling of displacive transformations. J. Mech. Phys. Solids 114, 117–142.

Ubachs, R.L.J.M., Schreurs, P.J.G., Geers, M.G.D., 2004. A nonlocal diffuse interface model for microstructure evolution of tin–lead solder. J. Mech. Phys. Solids 52, 1763–1792.

Waffenschmidt, T., Polindara, C., Menzel, A., Blanco, S., 2014. A gradient-enhanced large-deformation continuum damage model for fibre-reinforced materials. Comput. Meth. Appl. Mech. Eng. 268, 801–842.

Wang, Y., Khachaturyan, A.G., 1997. Three-dimensional field model and computer modeling of martensitic transformations. Acta Mater. 45, 759–773.

Wen, Y., Wang, Y., Chen, L.-Q., 2000. Phase-field simulation of domain structure evolution during a coherent hexagonal-to-orthorhombic transformation. Philos. Mag. A 80, 1967–1982.

Wriggers, P., 2006. Computational Contact Mechanics. Springer, Berlin Heidelberg New York.

Wulfinghoff, S., Böhlke, T., 2012. Equivalent plastic strain gradient enhancement of single crystal plasticity: theory and numerics. Proc. Roy. Soc. A 468, 2682–2703.

Zhao, P., Low, T.S.E., Wang, Y., Niezgoda, S.R., 2020. Finite strain phase-field microelasticity theory for modeling microstructural evolution. Acta Mater. 191, 253–269.

Zhong, Y., Zhu, T., 2014. Phase-field modeling of martensitic microstructure in NiTi shape memory alloys. Acta Mater. 75, 337–347.